

Article

# Comparison of Magma Oxygen Fugacity and Zircon Hf Isotopes between Xianglushan Tungsten-Bearing Granite and Late Yanshanian Granites in Jiangxi Province, South China

Xing-Yuan Li <sup>1,2</sup> , Jing-Ru Zhang <sup>1,3,\*</sup> and Chun-Kit Lai <sup>4,5</sup><sup>1</sup> School of Geography and Planning, Sun Yat-sen University, Guangzhou 510275, China; [lixingyuan@mail.sysu.edu.cn](mailto:lixingyuan@mail.sysu.edu.cn)<sup>2</sup> Department of Geology, University of Regina, Regina, SK S4S 0A2, Canada<sup>3</sup> Guangdong Province Academic of Environmental Science, Guangzhou 510045, China<sup>4</sup> Faculty of Science, Universiti Brunei Darussalam, Gadong BE1410, Brunei; [chunkit.lai@ubd.edu.bn](mailto:chunkit.lai@ubd.edu.bn)<sup>5</sup> Centre of Excellence in Ore Deposits (CODES), University of Tasmania, Tasmania 7001, Australia\* Correspondence: [zhjingru@mail.sysu.edu.cn](mailto:zhjingru@mail.sysu.edu.cn); Tel.: +86-020-8411-2307

Received: 2 December 2019; Accepted: 24 January 2020; Published: 26 January 2020



**Abstract:** Jiangxi Province (South China) is one of the world's top tungsten (W) mineral provinces. In this paper, we present a new LA-ICP-MS zircon U-Pb age and Hf isotope data on the W ore-related Xianglushan granite in northern Jiangxi Province. The magmatic zircon grains (with high Th/U values) yielded an early Cretaceous weighted mean U-Pb age of  $125 \pm 1$  Ma ( $MSWD = 2.5, 2\sigma$ ). Zircon  $\epsilon_{Hf}(t)$  values of the Xianglushan granite are higher ( $-6.9$  to  $-4.1$ , avg.  $-5.4 \pm 0.7$ ) than those of the W ore-related Xihuashan granite in southern Jiangxi Province ( $-14.9$  to  $-11.2$ , avg.  $-12.5 \pm 0.9$ ), implying different sources between the W ore-forming magmas in the northern and southern Jiangxi Province. Compiling published zircon geochemical data, the oxygen fugacity ( $fO_2$ ) of the late Yanshanian granitic magmas in Jiangxi Province (the Xianglushan, Ehu, Dahutang, and Xihuashan plutons) were calculated by different interpolation methods. As opposed to the W ore-barren Ehu granitic magma, the low  $fO_2$  of the Xianglushan granitic magma may have caused W enrichment and mineralization, whilst high  $fO_2$  may have led to the coexistence of Cu and W mineralization in the Dahutang pluton. Additionally, our study suggests that the absence of late Mesozoic Cu-Mo mineralization in the Zhejiang, Jiangxi, and Anhui Provinces (Zhe-Gan-Wan region) was probably related to low  $fO_2$  magmatism in the Cretaceous.

**Keywords:** Xinaglushan (Jiangxi); tungsten ore formation; oxygen fugacity; zircon Hf isotopes; South China

## 1. Introduction

South China (especially Jiangxi Province) is the main tungsten (W)-producing province in China. The early-discovered W deposits are mainly distributed in southwest Jiangxi Province, such as the renowned Xihuashan, Piaotang, and Dajishan deposits [1–5]. Xianglushan deposit was discovered in the 1960s in the northern Jiangxi province, a region better known for its association with world class porphyry copper (Dexing copper deposit (DCP)) and large- to medium-sized polymetallic Cu deposits [6–12]. The recent discovery of several super-large W deposits, such as the Zhuxi and Dahutang deposits in northern Jiangxi Province, have renewed research interest on the W metallogeny in the region and its relationship with the coeval Cu mineralization. Although the main W mineralization in both northern and southern Jiangxi Province was related to the Yanshanian (Jurassic-Cretaceous)

orogeny, there are obvious metallogenic differences between them. For instance, wolframite is the main W ore mineral in southern Jiangxi Province [5,10,13], while it is mainly scheelite in northern Jiangxi Province. Moreover, in northern Jiangxi Province, W mineralization coexists locally with Cu ± Mo and the reason for such differences is still unknown.

Advances in micro-analysis have resulted in the routine in-situ measurement of key geochemical and isotopic traits of zircons grains. Over the past few decades, there has been increasing interest in the use of zircon as a mineralization pathfinder for intrusion-related mineralization [14]. In this paper, zircon data from one ore-barren (Ehu) and two fertile granites (Dahutang and Xihuashan; Table A1) are compiled, and a new zircon U-Pb ages and Hf isotope data from the Xianglushan W bearing granite in northern Jiangxi Province are presented. We compared the age, oxygen fugacity ( $f\text{O}_2$ ), and possible magma source of the Xianglushan granite with those of the three other granite plutons and discussed the magmatic controls on W and W-Cu mineralization in the region. Our work also provides better understanding for the W mineralization during the Yanshanian period in Jiangxi Province.

## 2. Geological Background

### 2.1. Regional Geology

The South China Block (SCB) is composed of Yangtze and Cathaysia blocks separated along the Qin-Hang belt (Figure 1; [15,16]). Many previous studies proposed that the two blocks may have collided in the early Neoproterozoic, separated in the late Neoproterozoic, and then reassembled in the early Paleozoic (Caledonian) [3–7,15]. The SCB has since then experienced intensive and multiphase thermotectonic events [15,16], including those occurred in the Triassic (Indosinian) and Jurassic-Cretaceous (Yanshanian) [15,16]. Granites that formed during the Yanshanian orogeny are the most widespread, especially in the Cathaysia Block and the Qin-Hang belt. Moreover, there is a progressive coastward magmatic migration trend from the early to late Yanshanian orogeny [17–19].

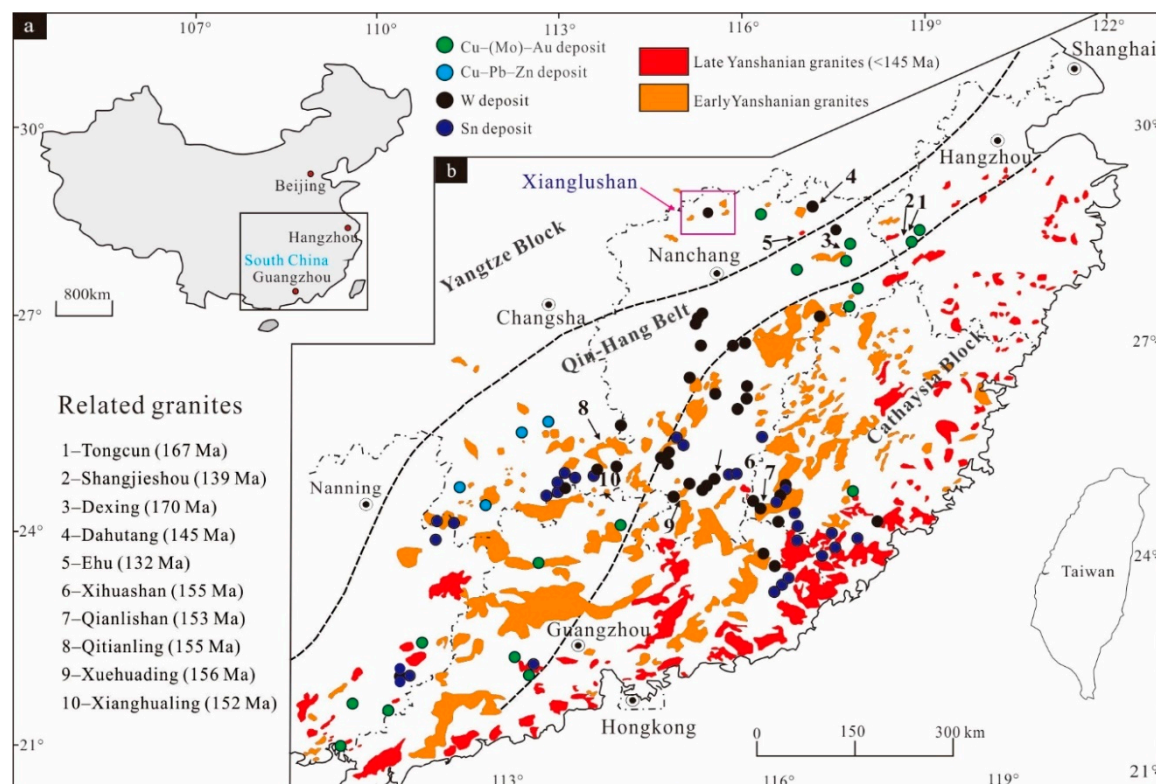


**Figure 1.** (a) Sketched map of China. (b) Simplified geological map, showing the distribution of Yanshanian granites in South China and its associated ore deposits (modified after [18,20]).

Neoproterozoic and late Mesozoic (Jurassic-Cretaceous; Yanshanian) granitoids are widespread in northern Jiangxi Province, and the latter occurs mainly as stocks intruding both the former and other Precambrian rocks [21,22]. In contrast, the Nanling Range extends across the northwestern Cathaysia Block [23] and encompasses southern Jiangxi Province, southern Hunan, and western Fujian Provinces. The Nanling Range includes a Neoproterozoic schist basement and Sinian–Silurian slate [18], which are covered by Upper Devonian to Middle Triassic shallow-marine carbonate rocks, mudstones, and sandstones, and then by Upper Triassic to Paleogene terrigenous clastic rocks and volcaniclastic rocks. Two world-class W ore belts were developed in the Nanling Range [8,10,13] and northern Jiangxi Province, respectively [10]. Southern Jiangxi Province is located in the eastern Nanling Range, including Xuehuading, Xianghualing, Qianlishan, and Xihuashan deposits. The northern Jiangxi Province contains the Dahutang W-Cu, Zhuxi W-Cu, and Xianglushan W deposits (Figure 1).

## 2.2. Petrology of Fertile/Barren Granites

The Xianglushan skarn W deposit in northwestern Jiangxi Province was discovered in 1958. The deposit has an ore reserve of 220 thousand tonnes (kt) at 0.641%  $\text{WO}_3$ . Local exposed sequences include the Cambrian Yangliugang Formation and upper member of the Huayansi Formation (Figure 2). These sequences mainly comprise well-bedded carbonaceous/cherty/muddy limestones and marl [24]. The Late Yanshanian biotite granite is the ore bearing rock, which is exposed in northeastern Xianglushan mining area, and dips gently to the southwest along the anticlinal limbs. Biotite granite is light-gray to white, and has quartz (55–60%), K-feldspar (~20%), plagioclase (10–15%), and biotite (5–10%) as its major constituents. Its accessory minerals include ilmenite, apatite, zircon, and titanite.

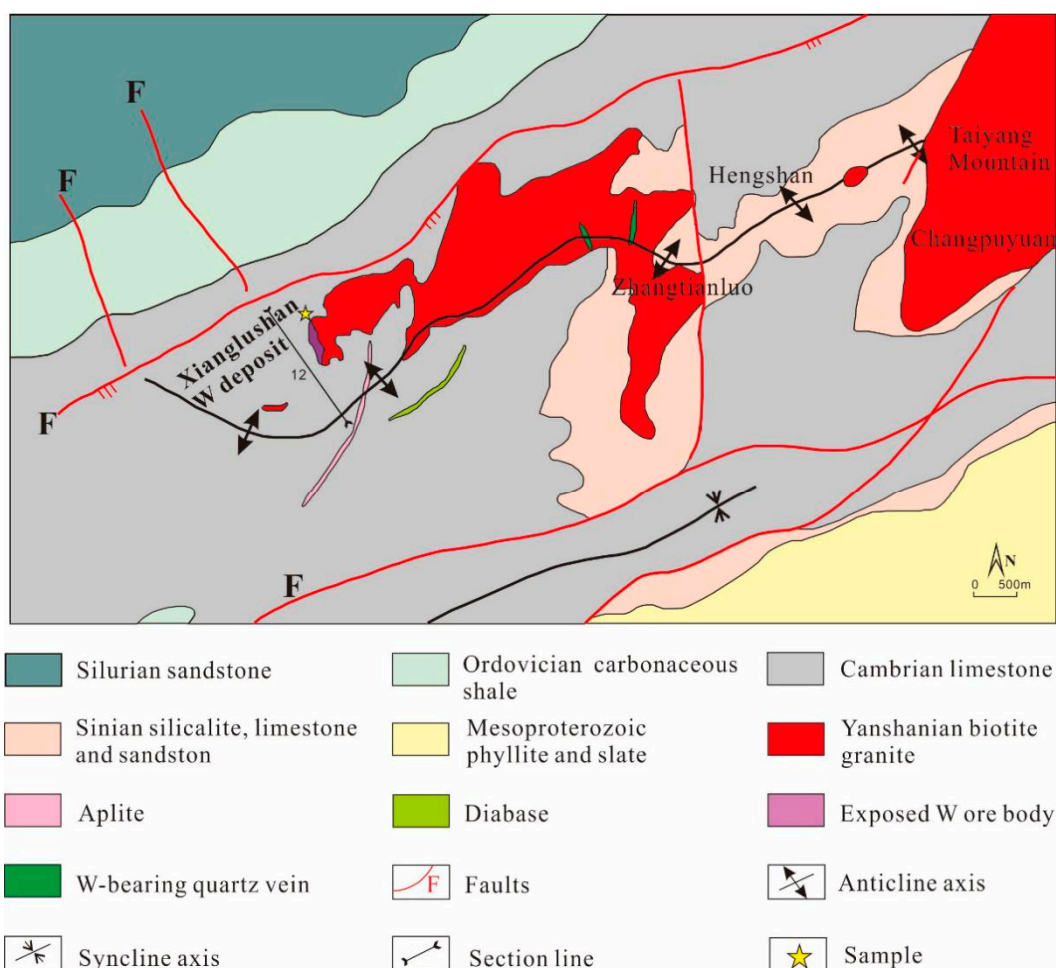


**Figure 2.** Simplified geologic map of the Xianglushan deposit (modified from [24,25]).

The Ehu pluton is located at about 30 km northeast of Jingdezhen and covers an area about 160 km<sup>2</sup>. The pluton is located on the southeastern margin of the Yangtze plate (Figure 1). The Ehu granite intruded the low-grade meta-sedimentary rocks of the Shuangqiaoshan Group. It consists of massive medium-grained two-mica granites with an association of monzogranite-syenogranite. The rocks are mainly composed of K-feldspar (35–40%), quartz (30%), plagioclase (24%), biotite (5%), and muscovite. Most of the plagioclase grains are sericitized and biotite is partially replaced by chlorite. Accessory minerals include mainly zircon, apatite, epidote, and Fe-Ti oxides. Moreover, the Ehu granites are devoid of Cu (Au)-Mo or Sn-W mineralization [26].

The Shimensi W polymetallic deposit is the largest deposit in the Dahutang ore field with a reserve of 0.74 Mt WO<sub>3</sub>, 403.6 kt Cu, and 28 kt Mo. Late Mesozoic granitic stocks and dikes are widely exposed in the Dahutang mining area and are considered to be W-Cu ore-related. These granites were emplaced into the Jiuling granodiorite batholith and Neoproterozoic Shuangqiaoshan Group, including porphyritic granite (dominant), fine-grained granite, and granite porphyry. The porphyritic granite has 30% quartz, 40%–45% K-feldspar, 5%–10% plagioclase, 10% biotite, and 5%–10% muscovite, and accessory apatite, zircon, fluorite, ilmenite, scheelite, and wolframite. The fine-grained granite intruded mainly the porphyry granite and locally the Neoproterozoic granite. The rocks have 30% quartz, 45% K-feldspar, 10% plagioclase, 10% biotite, and 5%–10% muscovite, and accessory zircon, fluorite, apatite, and ilmenite. Meanwhile, the granite porphyry dykes are distributed throughout the Shimensi deposit. They intruded both the porphyritic and fine-grained granites. Granite porphyry has 40% quartz, 40% feldspar, 5%–10% plagioclase, 5% biotite, and 5%–10% muscovite, as well as accessory zircon, apatite and fluorite. The three granites are interpreted as highly evolved S-type granites [5,27].

The Xihuashan pluton (outcrop size: 19.12 km<sup>2</sup>) is exposed in the Xihua Mountain and Dangping area, and intruded Cambrian sandstone and slate. The pluton is composed of medium-grained porphyritic/equigranular biotite granite and fine-grained two-mica granite, which are strongly peraluminous and belong to high-K S-type. The W-mineralized veins are spatially associated with the medium-grained biotite granite, which has plagioclase (~52%), quartz (~30%), alkali feldspar (~15%), biotite (~3%), and accessory minerals including zircon, apatite, monazite, xenotime, thorite, gadolinite, fluorite, and doverite [28].

### 3. Methods

#### 3.1. Zircon Morphology and Texture

Zircon separation was conducted on a ~2 kg crushed rock sample (XLS01-1) at the Hongxing Geological Laboratory (Langfang, China). After heavy liquid and electromagnetic separation, zircon grains with better crystal shape and transparency were picked under the microscope. The internal structure of zircon grain was observed via cathodoluminescence (CL) imaging and transmitted-/reflected-light microscopy. All of the CL imaging were conducted at the Wuhan Sample Solution Analytical Technology Co. Ltd. (Wuhan, China). Zircon CL images were obtained using an Analytical Scanning Electron Microscope (JSM-IT100) connected to a GATAN MINICL system. The imaging condition was 10.0–13.0 kV accelerating voltage of electric field and 80–85 µA current of tungsten filament.

#### 3.2. Zircon U-Pb Dating

LA-ICP-MS zircon U-Pb dating and trace element analysis were simultaneously conducted at the same laboratory as zircon CL imaging. The analyses were performed with a GeolasPro laser ablation system that consists of a COMPexPro 102 ArF excimer laser (193 nm wavelength and maximum 200 mJ energy) and a MicroLas optical system. Helium was used as a carrier gas, and argon as the make-up gas that mixed with helium via a T-connector before entering the ICP. A “wire” signal smoothing device was included in this laser ablation system [29,30]. The laser spot size and frequency were set to 32 µm and 5 Hz, respectively, and Plešovice zircon was used as the external standard. The obtained

Plešovice ( $338.6 \pm 1.1$  Ma) ages are consistent with the value reported by [31]. The off-line selection and background-analyzed signal integration, trace element calibration, and time-drift correction were performed with the in-house (CUG, Wuhan, China) ICPMSDataCal software (Version 10.9) [30]. Common Pb correction was carried out using with the measured  $^{204}\text{Pb}$  contents [32]. Concordia diagrams and weighted mean calculations were plotted with the Isoplot/Ex\_ver3 [33].

### 3.3. Zircon Hf Isotopic Analyses

In-situ Hf isotope analysis was conducted using a Neptune Plus MC-ICP-MS (Thermo Fisher Scientific, Dreieich, Germany) coupled with a Geolas HD excimer ArF laser ablation system (Coherent, Göttingen, Germany) at the same laboratory as the zircon U-Pb dating. Analysis conditions include 44  $\mu\text{m}$  spot size, 8 Hz laser repetition, and 5.3 J/cm<sup>2</sup> energy density, and other details are as described in Hu et al. [30]. Spot locations of the Hf isotopic analyses are shown in Figure 3. The analysis requires careful correction of isobaric interferences on  $^{176}\text{Hf}$  (e.g.,  $^{176}\text{Yb}$  and  $^{176}\text{Lu}$ ). It is observed that the mass fractionation of Yb ( $\beta\text{Yb}$ ) is not constant over time, and the  $\beta\text{Yb}$  obtained from the solution introduction is unsuitable for the measurements [34]. The  $\beta\text{Yb}$  miscalculation would affect the  $^{176}\text{Hf}/^{177}\text{Hf}$  results. In this study, we used the  $\beta\text{Yb}$  values directly obtained (real-time) from the zircon grains. Additionally, the  $^{173}\text{Yb}/^{171}\text{Yb}$  and  $^{179}\text{Hf}/^{177}\text{Hf}$  values were applied to estimate the mass bias of Yb ( $\beta\text{Yb}$ ) and Hf ( $\beta\text{Hf}$ ), which were normalized to  $^{173}\text{Yb}/^{171}\text{Yb}$  (1.13268) and  $^{179}\text{Hf}/^{177}\text{Hf}$  (0.73255) [35] with an exponential correction. Meanwhile, interference of  $^{176}\text{Yb}$  on  $^{176}\text{Hf}$  was corrected by measuring the interference-free  $^{173}\text{Yb}$  and utilizing  $^{176}\text{Yb}/^{173}\text{Yb}$  (0.79639) [35] to calculate  $^{176}\text{Yb}/^{177}\text{Hf}$ . Similarly, the relatively minor interference of  $^{176}\text{Lu}$  on  $^{176}\text{Hf}$  was corrected by measuring the interference-free  $^{175}\text{Lu}$  intensity and used  $^{176}\text{Lu}/^{175}\text{Lu}$  (0.02656) to estimate  $^{176}\text{Lu}/^{177}\text{Hf}$ . Since Yb and Lu have similar elemental behaviors,  $\beta\text{Yb}$  was applied to calculate the mass fractionation of Lu. The off-line processing of analytical data (e.g., mass bias calibration, sample selection, and blank signal) were performed with the ICPMSDataCal software [30]. Our analyses yielded weighted mean  $^{176}\text{Hf}/^{177}\text{Hf}$  ratios of  $0.2820172 \pm 0.0000060$  for the GJ-1 zircon standard and  $0.2823080 \pm 0.0000035$  for the 91500-zircon standard.

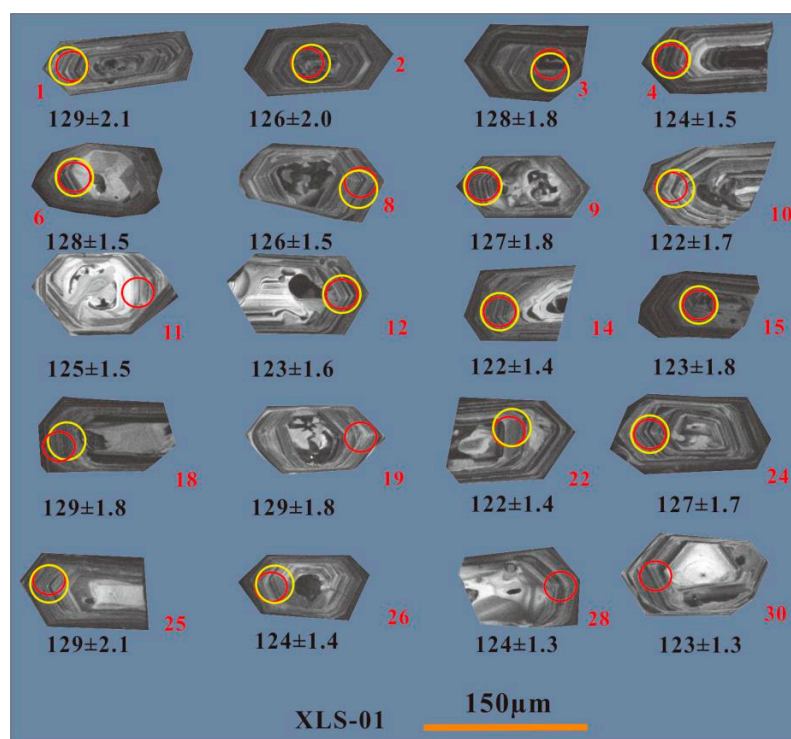


**Figure 3.** Representative zircon CL images of the Xianglushan biotite granite (sample XLS01-01). The yellow and red circles denote the Hf and U-Pb isotopic analysis spots, respectively.

### 3.4. Zircon Log $fO_2$ Ratios, Ce and Eu Anomaly Estimation

Zircon has high closure temperature and is resistant to weathering or hydrothermal alteration. In general, Ce in magma has two valence states ( $Ce^{4+}$  and  $Ce^{3+}$ ). Compared to  $Ce^{3+}$ ,  $Ce^{4+}$  has the same ionic radius and valence state as  $Zr^{4+}$  in the zircon lattice. Therefore,  $Ce^{4+}$  (instead of  $Ce^{3+}$ ) is compatible in magmatic zircon, which thus show strong positive Ce anomaly in chondrite-normalized REE (Rare Earth element) pattern. Various zircon Ce-based oxygen fugacity ( $fO_2$ ) indicators were developed to assess the magmatic redox conditions. In particular, Trail et al. [36] proposed an equation (Equation (1)) that can directly calculate the absolute value of oxygen fugacity. This equation has been widely adopted in many studies on the genesis of world-class porphyry Cu deposits:

$$\ln\left(\frac{Ce}{Ce^*}\right)_D = 0.1156 \pm 0.0050 \times \ln(fO_2) + \frac{13,860 \pm 708}{T(K)} - 6.125 \pm 0.484 \quad (1)$$

where  $(Ce/Ce^*)_D$  is the zircon Ce anomaly estimated from the partition coefficients and T is the absolute zircon crystallization temperature.

Recent studies suggested [37,38] that substitution of Ti,  $Si^{4+}$ , and  $Zr^{4+}$  in zircon lattice depends primarily on temperature. As a result, the titanium content can estimate zircon crystallization temperature, if the  $TiO_2$  and  $SiO_2$  activities in the melt at the time of crystallization are well constrained. Therefore, Equation (2) proposed by Ferry and Watson [37] was used to calculate the magma temperature at the time of zircon crystallization.

$$\log(ppm\ Ti-in-zircon) = (5.711 \pm 0.072) - \frac{4800 \pm 86}{T(K)} - \log \alpha_{SiO_2} + \log \alpha_{TiO_2} \quad (2)$$

where  $\alpha_{SiO_2}$  and  $\alpha_{TiO_2}$  represent the Si and Ti activity, respectively.

Notably, the studies of natural samples and experiments by Trail et al. [36] suggested that Ce anomalies in the magma can be calculated by the following approximation:

$$(Ce/Ce^*)_{CHUR} = \frac{D_{Ce}^{zrc/melt}}{\sqrt{D_{La}^{zrc/melt} \times D_{Pr}^{zrc/melt}}} \approx \frac{D_{Ce}^{zrc/chur}}{\sqrt{D_{La}^{zrc/chur} \times D_{Pr}^{zrc/chur}}} \quad (3)$$

CHUR is the abbreviation of chondrite uniform reservoir, where  $(Ce/Ce^*)_{CHUR}$  represents the Ce anomalies normalized to the chondritic uniform reservoir (CHUR; [39,40]). However, the measurement of  $Ce/Ce^* = Ce_N/(La_N^*Pr_N)^{1/2}$  (subscript N indicates chondrite normalization) anomaly is difficult because La and Pr are very difficult to be measured precisely. Moreover, the two elements are susceptible to contamination by tiny melt and titanite inclusions that are common in zircon [38]. This has led some authors to use a ratio between Ce and a more abundant REE as a proxy for Ce enrichment or depletion (such as  $Ce/Nd$ ; e.g., [40–42]. Loard et al. [43] argued that  $Ce/Ce^*$  can be estimated based on Equation (5), in which Sm and Nd were less affected by the inclusions and can be measured more precisely. Thus, determination of the Ce anomaly and  $fO_2$  for the magmas using the Sm-Nd interpolation can yield more robust  $fO_2$  values.

$$Nd_N \approx \sqrt{Ce^* \times Sm_N} \quad (4)$$

$$Ce^* \approx \frac{Nd_N^2}{Sm_N} \quad (5)$$

Furthermore, zircon  $Eu_N/Eu_N^*$  ratios can also evaluate the magmatic oxygen fugacity, because  $Eu^{2+}$  cannot substitute into zircon due to its cationic size and charge [42]. However, the redox effect on zircon  $Eu_N/Eu_N^*$  ratios is complicated by the strong partitioning of  $Eu^{2+}$  into other minerals, notably plagioclase [36,38,40]. Plagioclase crystallization can deplete the melt in Eu relative to Sm and Gd [43].

Hence, zircon Eu anomalies are not only influenced by redox, but also by the plagioclase abundance. In view of this, Eu anomaly is not used to assess the  $fO_2$  of granitic magmas in this study.

#### 4. Results

##### 4.1. Zircon U-Pb Age

Zircon grains separated from XLS01-1 sample are colorless, euhedral transparent, and about 50 to 150  $\mu\text{m}$  long. Most zircon grains have fine oscillatory zoning and some are sector-zoned (Figure 3). A total of 39 zircon grains from the sample were analyzed (Table 1) and their U and Th contents and Th/U ratios are of 255 to 8210 ppm, 244 to 1268 ppm, and 0.15 to 1.12, respectively (Table 1), resembling typical magmatic zircons ( $\text{Th}/\text{U} > 0.1$ , [12]). U-Pb ages of the zircon grains are highly consistent (122 to 129 Ma), which yielded a weighted-mean age of  $125 \pm 1$  Ma ( $n = 40$ , MSWD = 2.5; Figure 4), representing the crystallization age of the biotite granite XLS01-1.

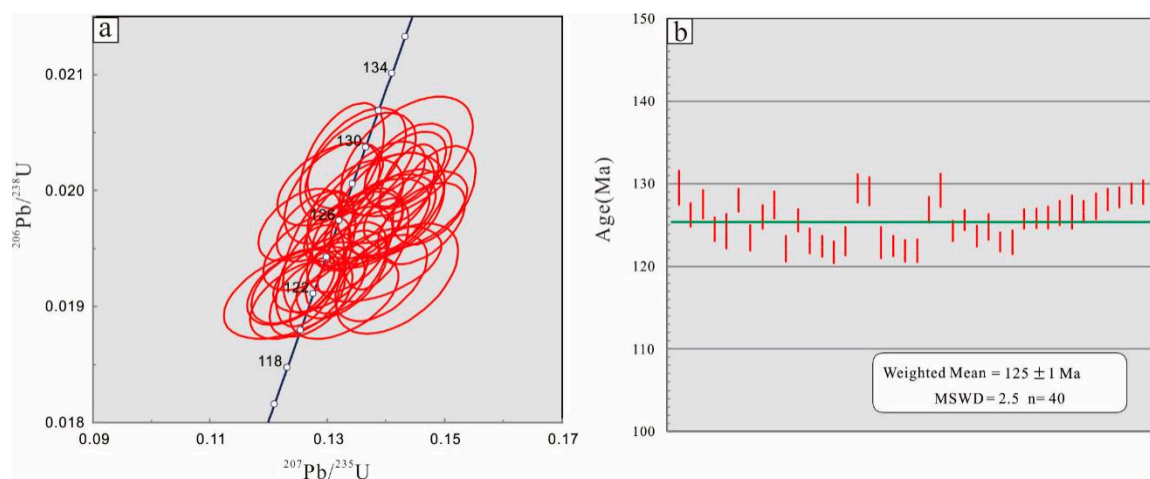


**Figure 4.** (a) Zircon U-Pb concordia and (b) weighted mean age diagrams for the Xianglushan biotite granite.

**Table 1.** Zircon U-Pb isotopic compositions and ages of the Xianglushan biotite granite ("PLE" represent the "Plesovice zircon").

Samples	Composition (ppm)			Isotopic Ratio				Isotopic Age (Ma)			
	Th	U	Th/U	$^{207}\text{Pb}/^{235}\text{U}$		$^{206}\text{Pb}/^{238}\text{U}$		$^{207}\text{Pb}/^{235}\text{U}$		$^{206}\text{Pb}/^{238}\text{U}$	
				Ratio	1σ	Ratio	1σ	Age	1σ	Age	1σ
1	595	704	0.85	0.1436	0.0074	0.0203	0.0003	136	6.6	129	2.1
2	589	790	0.75	0.1396	0.0059	0.0198	0.0002	133	5.2	126	1.5
3	841	925	0.91	0.1309	0.0054	0.0200	0.0003	125	4.8	128	1.8
4	780	953	0.82	0.1339	0.0048	0.0195	0.0002	128	4.3	124	1.5
5	599	2267	0.26	0.1286	0.0041	0.0195	0.0003	123	3.7	124	2.2
6	388	619	0.63	0.1305	0.0059	0.0201	0.0002	125	5.3	128	1.5
7	681	733	0.93	0.1333	0.0046	0.0193	0.0003	127	4.1	123	1.6
8	633	631	1.00	0.1386	0.0059	0.0197	0.0002	132	5.3	126	1.5
9	602	848	0.71	0.1483	0.0047	0.0200	0.0003	140	4.1	127	1.8
10	541	590	0.92	0.1244	0.0079	0.0191	0.0003	119	7.2	122	1.7
11	547	703	0.78	0.1352	0.0052	0.0197	0.0002	129	4.6	126	1.5
12	652	833	0.78	0.1325	0.0051	0.0193	0.0003	126	4.6	123	1.6
13	1016	910	1.12	0.1243	0.0052	0.0192	0.0002	119	4.7	122	1.4
14	400	691	0.58	0.1249	0.0054	0.0191	0.0002	120	4.8	122	1.4
15	1191	1784	0.67	0.1271	0.0039	0.0193	0.0003	122	3.5	123	1.8
16	546	940	0.58	0.1350	0.0055	0.0203	0.0003	129	5.0	129	1.8
17	381	615	0.62	0.1357	0.0062	0.0202	0.0003	129	5.5	129	1.8
18	586	670	0.87	0.1420	0.0068	0.0192	0.0003	135	6.1	123	2.0
19	1049	1057	0.99	0.1243	0.0047	0.0192	0.0002	119	4.3	122	1.3
20	855	996	0.86	0.1273	0.0047	0.0191	0.0002	122	4.2	122	1.4
21	592	589	1.01	0.1329	0.0061	0.0191	0.0002	127	5.4	122	1.5
22	730	775	0.94	0.1348	0.0054	0.0199	0.0003	128	4.8	127	1.7
23	692	937	0.74	0.1325	0.0048	0.0202	0.0003	126	4.3	129	2.1
24	504	675	0.75	0.1266	0.0049	0.0195	0.0002	121	4.4	124	1.4
25	543	699	0.78	0.1345	0.0055	0.0197	0.0002	128	5.0	126	1.3
26	484	575	0.84	0.1389	0.0070	0.0194	0.0002	132	6.2	124	1.3
27	1007	3696	0.27	0.1384	0.0036	0.0195	0.0003	132	3.2	125	1.7
28	537	764	0.70	0.1289	0.0053	0.0193	0.0002	123	4.8	123	1.3
29	793	1211	0.65	0.1393	0.0052	0.0192	0.0002	132	4.6	123	1.6
30	336	747	0.45	0.1280	0.0044	0.0197	0.0002	122	3.9	126	1.3
31	534	764	0.70	0.1252	0.0046	0.0197	0.0002	120	4.1	126	1.3

**Table 1.** *Cont.*

Composition (ppm)			Isotopic Ratio				Isotopic Age (Ma)				
Samples	Th	U	Th/U	Ratio	1σ	Ratio	1σ	Age	1σ	Age	1σ
32	962	1299	0.74	0.1461	0.0049	0.0197	0.0002	138	4.4	126	1.5
33	244	613	0.40	0.1418	0.0054	0.0198	0.0003	135	4.8	126	1.6
34	249	255	0.98	0.1383	0.0078	0.0198	0.0003	132	6.9	127	2.1
35	618	770	0.80	0.1451	0.0058	0.0198	0.0002	138	5.2	127	1.4
36	332	646	0.51	0.1400	0.0054	0.0199	0.0003	133	4.9	127	1.6
37	1268	8210	0.15	0.1440	0.0033	0.0201	0.0002	137	2.9	128	1.4
38	842	964	0.87	0.1395	0.0048	0.0201	0.0002	133	4.2	128	1.3
39	717	1013	0.71	0.1433	0.0046	0.0202	0.0002	136	4.1	129	1.3
40	1147	1244	0.92	0.1439	0.0049	0.0202	0.0002	136	4.3	129	1.5
PLE	140	929	0.15	0.3962	0.0117	0.0543	0.0005	339	8.5	341	3.2
PLE	137	928	0.15	0.3964	0.0127	0.0538	0.0005	339	9.2	338	3.4
PLE	140	921	0.15	0.4072	0.0098	0.0542	0.0005	347	7.1	340	2.9
PLE	48.1	491	0.10	0.4102	0.0123	0.0549	0.0005	349	8.9	345	3.3
PLE	79.3	795	0.10	0.3852	0.0109	0.0537	0.0006	331	8.0	337	3.4
PLE	77.4	786	0.10	0.3778	0.0113	0.0532	0.0006	325	8.3	334	3.7
PLE	145	917	0.16	0.4043	0.0100	0.0540	0.0004	345	7.3	339	2.7

#### 4.2. Zircon Hf Isotopes

Zircon Hf-isotopic data of the Xianglushan biotite granite (XLS01-1) were listed in Table 2. These zircon crystals have  $^{176}\text{Hf}/^{177}\text{Hf}$  ratios mainly range from 0.282513 to 0.282594. The zircon  $\varepsilon\text{Hf(t)}$  values of the Xianglushan biotite granite are characterized by a narrow initial range ( $-6.9$  to  $-4.1$ ; avg.  $-5.4 \pm 0.7$ ). In addition, the Hf-isotopic data show the younger two-stage model ages (TDM2) of 1085 to 1215 Ma (avg.  $1143 \pm 30$  Ma; Figure 5 and Table 2).

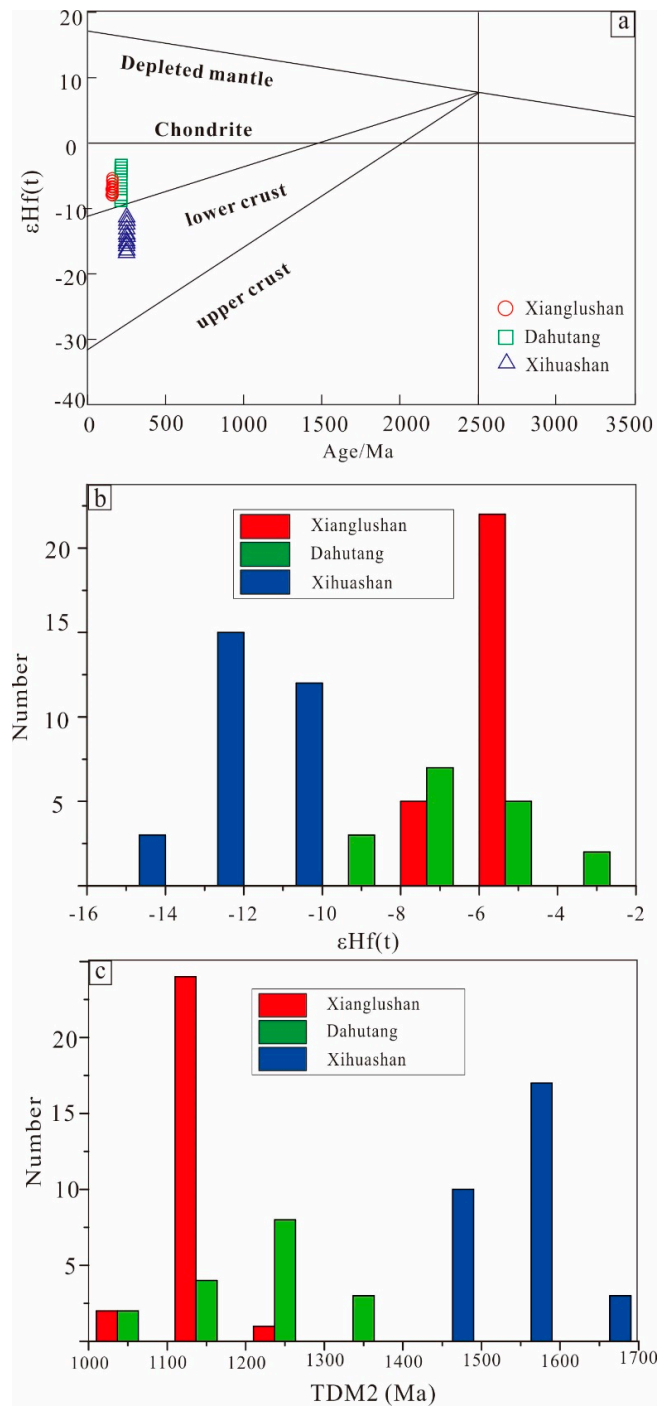


**Figure 5.** (a)  $\varepsilon\text{Hf(t)}$  vs. U-Pb age diagram and histograms of (b)  $\varepsilon\text{Hf(t)}$  value; (c) Two-stage model ages (TDM2).

**Table 2.** Zircon Hf isotopes of the Xianglushan biotite granite.

Samples	$^{176}\text{Hf}/^{177}\text{Hf}$	$1\sigma$	$^{176}\text{Lu}/^{177}\text{Hf}$	$1\sigma$	$^{176}\text{Yb}/^{177}\text{Hf}$	$1\sigma$	$\varepsilon\text{Hf(0)}$	$\varepsilon\text{Hf(t)}$	TDM2 (Ma)
XLS01-01	0.282568	0.000011	0.001965	0.00005	0.057096	0.001344	-7.6736743	-5.0	1127
XLS01-02	0.282544	0.000009	0.002183	0.000058	0.067082	0.001738	-8.5223757	-5.9	1168
XLS01-03	0.282552	0.000008	0.002332	0.000072	0.071557	0.001866	-8.2394752	-5.6	1155
XLS01-04	0.282559	0.00001	0.002042	0.000053	0.060775	0.001423	-7.9919373	-5.4	1143
XLS01-06	0.282561	0.000009	0.001585	0.000022	0.04803	0.000642	-7.9212122	-5.3	1137
XLS01-08	0.282576	0.00001	0.001691	0.000019	0.051412	0.000514	-7.3907739	-4.7	1113
XLS01-09	0.282577	0.000011	0.002001	0.000031	0.061653	0.000679	-7.3554114	-4.7	1112
XLS01-10	0.282538	0.000008	0.002075	0.000072	0.061922	0.00193	-8.734551	-6.1	1178
XLS01-12	0.28254	0.000009	0.001714	0.000055	0.051492	0.001585	-8.6638259	-6.0	1173
XLS01-14	0.282563	0.000009	0.001555	0.000049	0.046709	0.001414	-7.8504871	-5.2	1134
XLS01-15	0.282535	0.000009	0.002769	0.000056	0.084887	0.001648	-8.8406386	-6.3	1185
XLS01-18	0.282573	0.000009	0.00172	0.000016	0.05109	0.000402	-7.4968616	-4.8	1118
XLS01-22	0.282542	0.000009	0.002125	0.000085	0.064811	0.002413	-8.5931008	-6.0	1171
XLS01-24	0.282573	0.000013	0.001833	0.000029	0.055654	0.000636	-7.4968616	-4.9	1118
XLS01-25	0.282572	0.000011	0.001906	0.000043	0.057709	0.000925	-7.5322241	-4.9	1120
XLS01-26	0.282574	0.000009	0.00135	0.000022	0.040415	0.00073	-7.461499	-4.8	1115
XLS-05	0.282576	0.000016	0.001841	0.000027	0.061811	0.000767	-7.3964216	-4.8	1114
XLS-11	0.282545	0.000011	0.001343	0.000009	0.045204	0.000274	-8.4776856	-5.8	1163
XLS-12	0.282594	0.000017	0.002001	0.000009	0.067159	0.000373	-6.7633205	-4.1	1085
XLS-14	0.282513	0.000015	0.000950	0.000016	0.032482	0.000642	-9.620265	-6.9	1215
XLS-16	0.282556	0.000015	0.001317	0.000013	0.043197	0.000308	-8.1122868	-5.4	1145
XLS-18	0.282526	0.000017	0.001107	0.000007	0.036130	0.000360	-9.1530133	-6.4	1193
XLS-30	0.282585	0.000017	0.001688	0.000014	0.058506	0.000515	-7.074418	-4.4	1098
XLS-31	0.282555	0.000019	0.002039	0.000012	0.068353	0.000525	-8.1272529	-5.5	1149
XLS-32	0.282559	0.000014	0.001587	0.000027	0.053373	0.000873	-7.9958257	-5.3	1141
XLS-33	0.282553	0.000014	0.000614	0.000002	0.020463	0.000099	-8.2042643	-5.5	1147
XLS-35	0.282555	0.000015	0.001045	0.000007	0.034642	0.000237	-8.148415	-5.4	1146

Note:  $\varepsilon\text{Hf(t)} = 10,000 \times \{[({}^{176}\text{Hf}/{}^{177}\text{Hf})_S - ({}^{176}\text{Lu}/{}^{177}\text{Hf})_S \times (e^{At} - 1)] / ({}^{176}\text{Hf}/{}^{177}\text{Hf})_{\text{CHUR},0} - ({}^{176}\text{Lu}/{}^{177}\text{Hf})_{\text{CHUR}} \times (e^{At} - 1)\} - 1$ .  $({}^{176}\text{Lu}/{}^{177}\text{Hf})_{\text{CHUR}} = 0.0332$ ,  $({}^{176}\text{Hf}/{}^{177}\text{Hf})_{\text{CHUR},0} = 0.282772$ ,  $({}^{176}\text{Lu}/{}^{177}\text{Hf})_{\text{DM}} = 0.0384$  and  $({}^{176}\text{Hf}/{}^{177}\text{Hf})_{\text{DM}} = 0.28325$  [44–46]; Two-stage model age (TDM2) calculation after [46], and we used Lu/Hf = 0.042 (S-type granites with > 74 wt.% SiO<sub>2</sub>).

Similarly, the zircon  $\epsilon\text{Hf(t)}$  and TDM2 are of  $-10$  to  $-2.4$  (avg.  $-6.2 \pm 1.8$ ) and  $1042$  to  $1394$  Ma (avg.  $1221 \pm 86$  Ma) for the Dahutang ore-related granite [8]. Comparatively, the Xihuashan W ore-related granite has lower zircon  $\epsilon\text{Hf(t)}$  values ( $-14.9$  to  $-11.4$ , avg.  $-12.5 \pm 0.9$ ; [47,48]), which plot above the CHUR evolutionary line in the  $\epsilon\text{Hf(t)}$  vs. U-Pb age diagram (Figure 5a,b). Moreover, the Xihuashan granite shows the older TDM2, ranging from  $1473$  to  $1634$  Ma (avg.  $1525 \pm 43$  Ma; Figure 5c; Table A2).

#### 4.3. Temperature-Redox Conditions

Calculated Ti-in-zircon temperatures of the W-related granites from the three deposits and the Ehu ore-barren granite are listed in Table A1. The activities of  $\text{TiO}_2$  and  $\text{SiO}_2$  were estimated to be  $0.7$  and  $1$ , respectively. The Ti-in-zircon temperatures are  $666$  to  $786$  °C (avg.  $699 \pm 32$  °C) for the Xianglushan biotite granite,  $709$  to  $848$  °C (avg.  $745 \pm 35$  °C) for the Dahutang granite,  $654$  to  $890$  °C (avg.  $727 \pm 51$  °C) for the Xihuashan granite, and  $654$  to  $890$  °C (avg.  $727 \pm 33$  °C) for the Ehu granite.

The  $\log f\text{O}_2$  values for the W-related and barren granites were listed in Table A1 and illustrated in Figures 6 and 7. It is noted that the  $\log f\text{O}_2$  values were calculated by the La-Pr and Nd-Sm interpolation methods, respectively. As shown in Figure 6a, most data from the Xianglushan granite are located below those of the Ehu ore-barren granite.  $\log f\text{O}_2$  values range from FMQ  $-12.01$  to  $4.76$  (avg.  $-7.97 \pm 3.73$ ) for the bearing granite, and from FMQ  $-10.13$  to  $+7.59$  (avg.  $-2.36 \pm 4.32$ ) for the barren one (Figure 6b). Although the results are broadly consistent with the previous redox estimates for these zircons [37], our results indicate a slightly oxidizing environment. It is also noted that the  $\log f\text{O}_2$  range of Ehu granite in Figure 6c is narrower than that in Figure 6a. The results estimated by Equation (3) range from FMQ  $-13.00$  to  $+3.61$  (avg.  $-7.16 \pm 4.5$ ) for the ore-bearing granite, and from FMQ  $-6.01$  to  $+5.54$  (avg.  $-1.93 \pm 2.46$ ) for the barren granite (Table A1; Figure 6d).

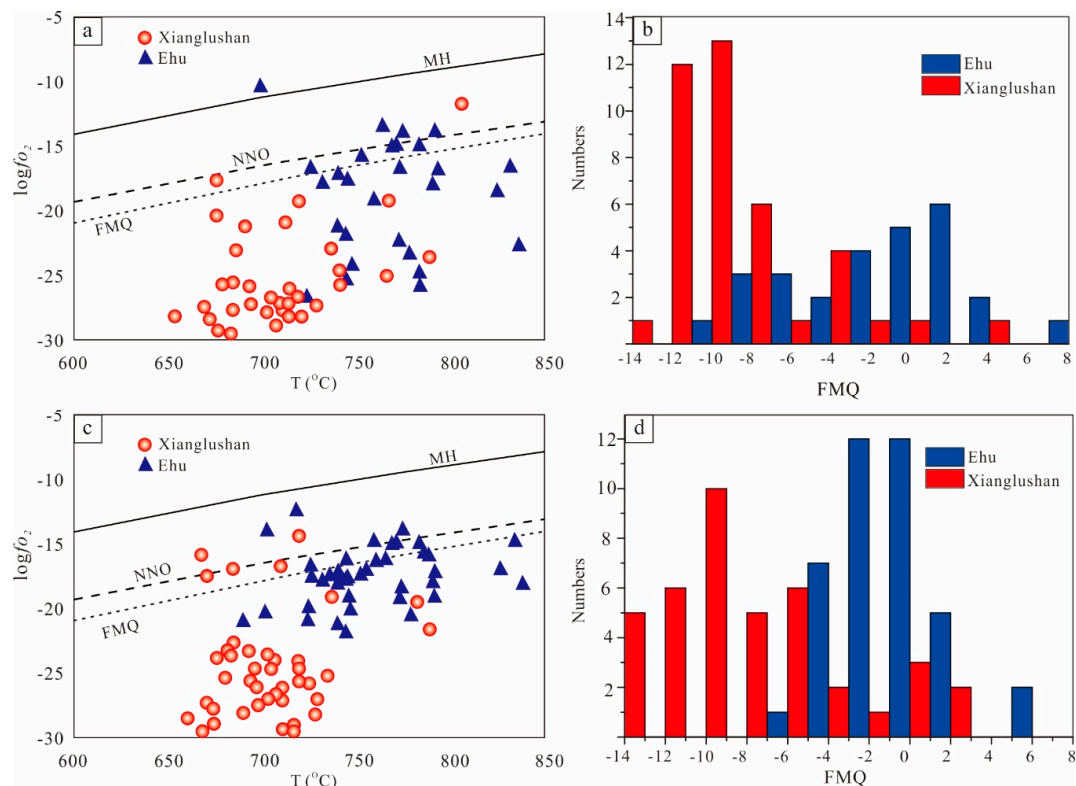


**Figure 6.**  $\log f\text{O}_2$ -related binary diagrams of zircon grains from the Xianglushan and Ehu granites (a)  $\log f\text{O}_2$  vs. temp diagram, where  $\log f\text{O}_2$  was calculated with the method of Trail et al. [37], and  $Ce_N^*$  by the La-Pr interpolation method; (b) Histogram of oxygen fugacity; (c)  $\log f\text{O}_2$  vs. temp diagram, where  $\log f\text{O}_2$  value was calculated by the method of Trail et al. [37], and  $Ce_N^*$  by the Sm-Nd fitting method; (d) Histogram of oxygen fugacity. Data are listed in Table A1.

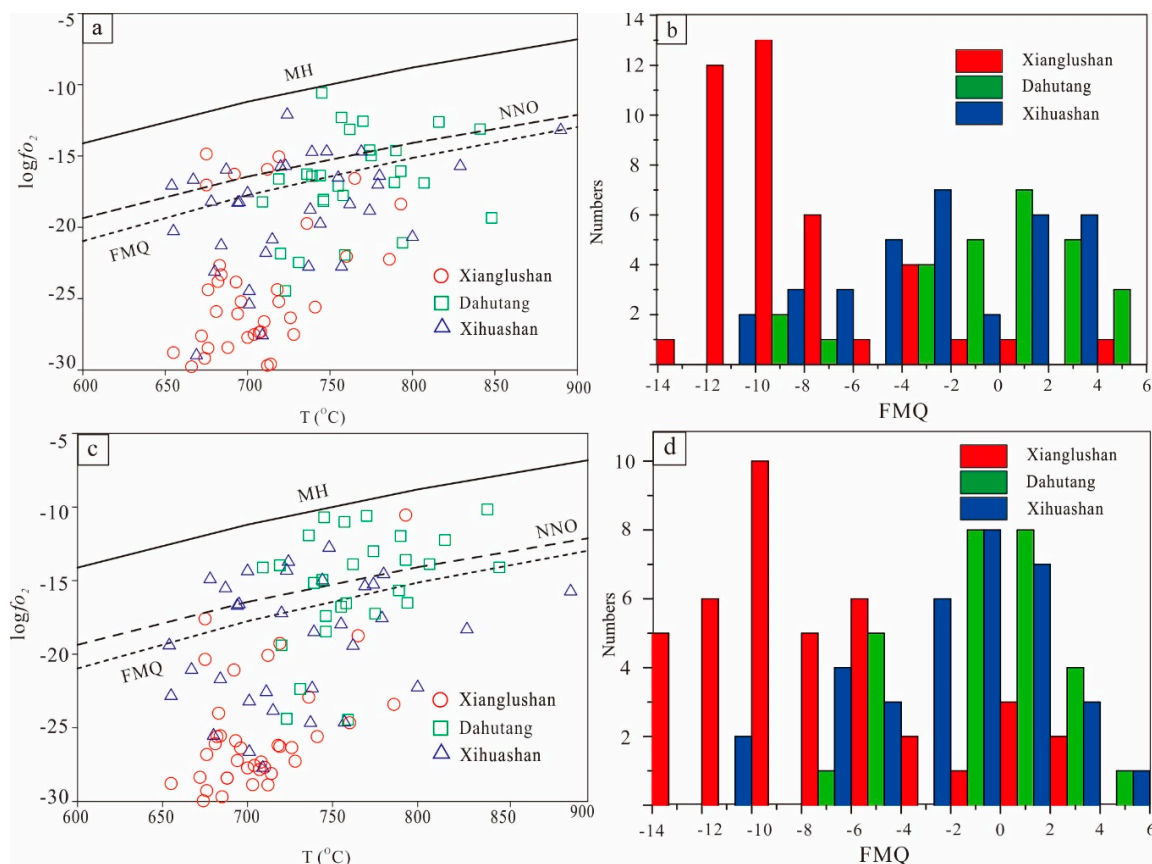


**Figure 7.**  $\log f\text{O}_2$ -related binary diagrams of zircon grains from the Xianglushan, Dahutang and Xihuashan granites. (a)  $\log f\text{O}_2$  vs. temp diagram, where  $\log f\text{O}_2$  value was calculated with the method of Trail et al. [34], and  $Ce_N^*$  with the La-Pr interpolation method; (b) Histogram of oxygen fugacity; (c)  $\log f\text{O}_2$  vs. temp diagram, where  $\log f\text{O}_2$  value was calculated with the method of Trail et al. [34], and  $Ce_N^*$  with the Sm-Nd fitting method; (d) Histogram of oxygen fugacity. Data are listed in Table A1.

As shown in Figure 7, although the Dahutang granite zircon data are partially overlapped with those from the Xihuashan and Xianglushan granites, zircon grains from the Dahutang ore-bearing granite still have the highest  $\log f\text{O}_2$  values regardless of the calculation method. The La-Pr interpolation approach yielded  $\log f\text{O}_2$  values of FMQ  $-9.34$  to  $+4.76$  (avg.  $-0.37 \pm 3.63$ ) for the Dahutang granite, FMQ  $-11.70$  to  $+3.33$  (avg.  $-2.80 \pm 4.33$ ) for the Xihuashan granite, and FMQ  $-12.01$  to  $4.76$  (avg.  $-7.97 \pm 3.73$ ) for the Xianglushan granite (Figure 7a,b). In contrast, the Sm-Nd interpolation method obtained a narrower  $\log f\text{O}_2$  range (Figure 7c,d), and higher values (albeit some overlapping) for the Dahutang (FMQ  $-7.33$  to  $+5.90$ ; avg.  $-0.79 \pm 3.27$ ) and Xihuashan (FMQ  $-10.29$  to  $+4.97$ ; avg.  $-1.92 \pm 3.67$ ) granites than the Xianglushan granite (FMQ  $-13.00$  to  $+3.61$ ; avg.  $-7.16 \pm 4.54$ ) (Figure 7; Table A1). Notably, unlike the La-Pr interpolation, the Sm-Nd fitting method does not require accurate measurement of La or Pr and is thus considered to be more robust. Meanwhile, some studies [25] further suggested that zircon REEs have a concave-downward (rather than linear) chondrite-normalized pattern. Hence, neither of the two methods can accurately determine  $Ce^*$  and would result in under-/over-estimation of the true  $Ce^*$ .

## 5. Discussion

### 5.1. Timing of Magmatism and its Related W Mineralization

LA-ICP-MS zircon U-Pb dating suggests that the Xianglushan granite was formed at  $125 \pm 1$  Ma, coeval to the W mineralization (scheelite Sm-Nd age:  $121 \pm 11$  Ma [23]). Moreover, the molybdenite

Re-Os age and  $^{40}\text{Ar}$ - $^{39}\text{Ar}$  dating of muscovite are also consistent with the U-Pb zircon age of  $125 \pm 1$  Ma for the biotite granite. On the basis of the LA-ICP-MS zircon U-Pb, molybdenite Re-Os, and muscovite  $^{40}\text{Ar}$ - $^{39}\text{Ar}$  ages [9,23], it is concluded that W mineralization at the Xianglushan deposit is genetically associated with the biotite granite. Magmatism and mineralization in the Xianglushan deposit occurred during the Early Cretaceous. Additionally, published age data indicate two late Mesozoic (Yanshanian) magmatic event in Jiangxi Province (Table 3; Figure 8): The first Late Jurassic-Early Cretaceous events occurred mainly at 160–140 Ma, e.g., the emplacement of ore-related granite (porphyries) at the Zhuxi W-Cu (148–152 Ma) and Xihuashan W deposits (158–161 Ma) [13]. The second event occurred mainly at 135–120 Ma, e.g., the Xianglushan granite (ca. 125 Ma; this study). It is noteworthy that both magmatic events were reported at the Dahutang W deposit (Table 3), and both events may have been ore-related [49,50]. In summary, the Yanshanian magmatism and its related W mineralization in southern Jiangxi Province occurred in a relatively confined period of time, while the magmatism and related W-Cu-(Mo) mineralization in northern Jiangxi Province are characterized by occurring as multi-phases at a wider age span.

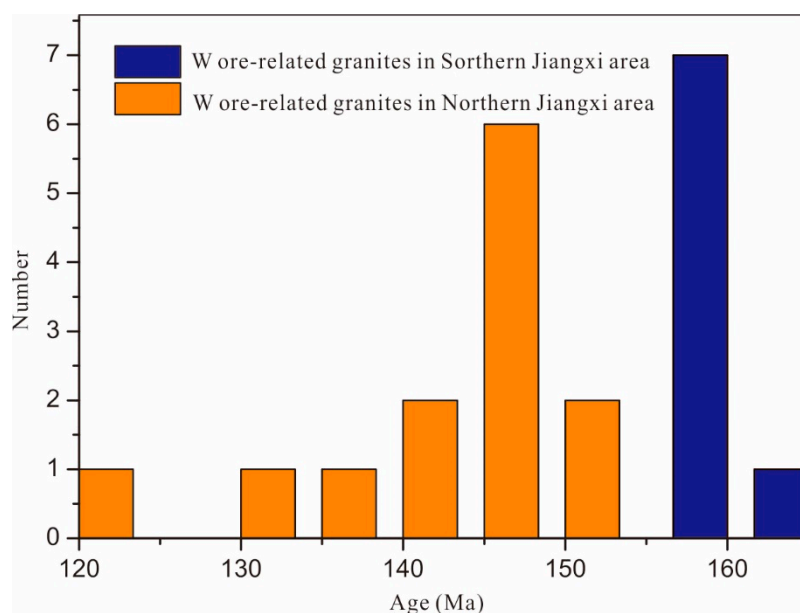


**Figure 8.** Histogram of granite ages in Jiangxi Province. Age data are listed in Table 3.

**Table 3.** Yanshanian granites and related W deposits in Jiangxi Province selected for this study.

Area	Deposit	Lithology	Age (Ma)	Method	Ref.	Mineralization Age (Ma)	Method	Ref.
Northern Jiangxi Province	Dahutang W-Cu deposit	Porphyritic muscovite granite	144 ± 1	Zircon LA-ICP-MS U-Pb	[47]	141 ± 4	Molybdenite Re-Os	[1]
		W-rich granite porphyry	135 ± 1	Zircon LA-ICP-MS U-Pb	[47]	142 ± 9	Scheelite Sm-Nd	[48]
		Porphyritic two-mica granite	144 ± 1	Zircon LA-ICP-MS U-Pb	[47]			
		Porphyry two-mica granite	130 ± 1	Zircon LA-ICP-MS U-Pb	[47]			
		Porphyritic biotite granite	138 Ma	Zircon LA-ICP-MS U-Pb	[49]	144 ± 1	Molybdenite Re-Os	[1]
		Granite porphyry	135 Ma	Zircon LA-ICP-MS U-Pb	[49]	150 ± 1	Molybdenite Re-Os	[49]
		Porphyritic biotite granite	147 ± 1	Zircon LA-ICP-MS U-Pb	[9]	139 ± 1	Molybdenite Re-Os	[20]
		Porphyritic biotite granite	148 ± 2	Zircon LA-ICP-MS U-Pb	[9]	144 ± 1	Molybdenite Re-Os	[48]
		Granule biotite granite	145 ± 1	Zircon LA-ICP-MS U-Pb	[9]			
		Granule biotite granite	146 ± 1	Zircon LA-ICP-MS U-Pb	[9]			
Zhuxi W-Cu deposit	Yangchuling W deposit	Granite porphyry	143 ± 1	Zircon LA-ICP-MS U-Pb	[9]			
		Granite porphyry	143 ± 1	Zircon LA-ICP-MS U-Pb	[9]			
		Muscovite granite	147 ± 1	Zircon LA-ICP-MS U-Pb	[50]			
		altered granite	149 ± 2	Zircon LA-ICP-MS U-Pb	[51]			
		Altered granite porphyry	148 ± 3	Zircon LA-ICP-MS U-Pb	[51]			
Xianglushan W deposit		Granite porphyry	151 ± 2	Zircon LA-ICP-MS U-Pb	[51]			
		Granite porphyry	150 ± 2	Zircon LA-ICP-MS U-Pb	[51]			
		Granite porphyry	146 ± 3	Zircon LA-ICP-MS U-Pb	[52]			
		biotite granite	120 ± 1	Zircon LA-ICP-MS U-Pb	[53]	121 ± 11		[54]
Southern Jiangxi Province	Xihuashan W deposit	Porphyry medium-grained biotite granite	159 ± 1	Zircon SIMS U-Pb	[13]	158 ± 1		[17]
		Garnet-bearing fine-grained biotite granite	161 ± 3	Zircon SIMS U-Pb	[13]	153 ± 2		[17]
		Garnet-bearing fine-grained porphyry biotite granite	159 ± 2	Zircon SIMS U-Pb	[13]			
		Fine-grained porphyry biotite granite	158 ± 2	Zircon SIMS U-Pb	[13]			
	Dangping W deposit	Porphyritic granite	159 ± 3	Zircon LA-ICP-MS U-Pb	[55]			
		Porphyry biotite granite	155 ± 2	Zircon LA-ICP-MS U-Pb	[55]			
		Medium-fine-grained porphyry granite	157 ± 2	Zircon LA-ICP-MS U-Pb	[55]			
		biotite granite	158 ± 2	Zircon LA-ICP-MS U-Pb	[55]			

### 5.2. $\epsilon\text{Hf}(t)$ Variation and Ore Material Source

Previous studies demonstrated that the W mineralization is closely related with Cu-(Mo) mineralization in northern Jiangxi Province, which is uncommon worldwide outside of South China [2,23,47]. Tungsten is an a lithophile element due to a valence of +6 in nature. Currently, over 20 W-bearing minerals (notably wolframite and scheelite) have been identified in nature [2,10,47,55,56]. The increase of oxygen content between the core and the mantle leads to the separation of tungsten from the core and its entry into the mantle [47,57]. Meanwhile, tungsten is an incompatible element and tends to accumulate in the crust during the crust mantle process and evolution. O'Neill et al. [57] reported that partition coefficients for W between silicate and Fe-rich metal will be highly increased under reduced condition. Unlike W, the oxidized magma is beneficial for Cu-(Au)-Mo mineralization through controlling the valence of sulfur. Thus, W and Cu tend to be enriched in the crust and mantle, respectively [10,12,18].

In this study, W-bearing granites from both the northern and southern Jiangxi Province have negative  $\epsilon\text{Hf}(t)$  values ( $-14.9$  to  $-2.4$ ). Moreover, the Hf two-stage model age vary from 1085 to 1634 Ma and the Hf two-stage model of the individual granite is relatively uniform in age, indicating that these granites may have mainly crustal source [47]. Meanwhile, the  $\epsilon\text{Hf}(t)$  values of ore-related granites in northern Jiangxi Province are clearly higher than those in southern Jiangxi Province. As shown in Figure 5c, compared to the ore-related granites in southern Jiangxi Province, those in northern Jiangxi Province have the younger TDM2 age which indicates the major source difference between the northern and southern magmas. This may have caused by partial melting of different metamorphic substrates [12,24,56]. According to the whole-rock geochemical data, granites in southern Jiangxi Province have higher  $\text{SiO}_2$ , but lower  $\text{Al}_2\text{O}_3$ ,  $\text{TiO}_2$  and  $\text{MgO}$ , and significantly lower  $\text{P}_2\text{O}_5$  contents. The A/CNK-A/NK diagram suggests that W ore-related granites from both southern and northern Jiangxi Province are peraluminous. In addition, the ore-bearing granites in southern Jiangxi Province have higher  $\text{Rb/Sr}$ , but lower  $\text{Zr/Hf}$ , LREE/HREE and  $\text{Eu/Eu}^*$  than their northern Jiangxi counterparts. By comparing the granite whole-rock  $^{87}\text{Sr}/^{86}\text{Sr}$  and  $\epsilon\text{Nd}(t)$  values from northern Jiangxi Province and those of the Neoproterozoic Shuangqiaoshan Group, Su and Jiang [48] proposed that the former may have partly originated from the latter, which contains much higher contents of W (avg. 9.13 ppm) and Cu (avg. 38.1 ppm) than the average continental crust (W: 1 ppm, Cu: 27 ppm; [47]). Comparatively, both the ore-related granites and wall-rock sequences in southern Jiangxi Province have high W background contents [47,48], which may have contributed some ore-forming materials for the (super)-large W mineralization in the region. Notably, differences in  $\text{Sr/Sr}$ , Nd and Hf isotopes of granites in north and south do indicate probable differences in the source [8,47]. But the geochemical characteristics as lower  $\text{Zr/Hf}$ ,  $\text{Eu/Eu}$ ,  $\text{Al}_2\text{O}_3$ ,  $\text{TiO}_2$ , and  $\text{MgO}$  or higher  $\text{SiO}_2$  and  $\text{Rb/Sr}$  might be most probably related to differences in the fractionation of these magmas [13,43,58], that is, this probably indicates that granites from the south are more evolved than those from the north.

### 5.3. Oxygen Fugacity Variation and Implications

Pirajno [59] proposed that the  $f\text{O}_2$  dependency of mineralization increases in the Sn-W-Mo-Cu-Mo-Cu-Au sequence, while the Fe dependency increases in the Mo-Sn-W-Cu-Mo-Cu-Au sequence. Nevertheless, the relationship between  $f\text{O}_2$  and W mineralization is still not fully understood [18]. Some workers believed that low  $f\text{O}_2$  is beneficial to W mineralization, whereas many others suggested that  $f\text{O}_2$  plays little role in the W mineralization. Although W mineralization shows little dependence on magma  $f\text{O}_2$  in view of geochemical affinity [60], large-scale W mineralization is always closely associated with reduced granites [18,47]. In our study, no matter which calculation method is used, the  $f\text{O}_2$  of the Xianglushan granite is always lower than that of the ore-barren Ehu granite. This suggests that lower  $f\text{O}_2$  may have been beneficial for W mineralization in northern Jiangxi, e.g., at Xianglushan. It may be explained by that low  $f\text{O}_2$  facilitates W enrichment in silicate melts during source melting and magmatic differentiation. However, as shown in Figure 7, Dahutang granite has the highest  $f\text{O}_2$ , and could be interpreted as having different magma sources. Based on

the Hf isotope evidence, the Dahutang ore-bearing granite in northern Jiangxi Province was probably sourced from arc-type materials (of the Shuangqiaoshan Group), which commonly have high  $\log fO_2$  values (NNO +1 to +3). Copper mineralization is generally associated with oxidized magmas [60–63] and can explain the coexistence of Cu and W mineralization in the northern Jiangxi Province.

Magma oxygen fugacity has been widely accepted as the most important control of Cu-Mo-Au mineralization (e.g., [5,8,47,64]). Many recent studies showed that high  $fO_2$  granitic magma is the key for Cu mineralization in northeastern Jiangxi Province. For example, the ore-related granites in the Dexing and Tongcun PCDs have likely high  $fO_2$  [11]. Meanwhile, Qiu et al. [26,62] suggested that the low magma  $fO_2$  found in several Mo ore-related and ore-barren porphyries in western Zhejiang Province may have contributed to the Cretaceous Cu-Mo mineralization gap in the Zhe-Gan-Wan region. This hypothesis is supported by our study, as shown in Figure 9 and Table 4, Nd-Sm interpolation approach yielded  $\log fO_2$  values of FMQ –10.29 to +11.87 (avg.  $+3.54 \pm 4.02$ ) for the Late Jurassic granites (145–170 Ma) FMQ –13.00 to –5.55 (avg.  $-3.69 \pm 4.70$ ) for the Early Cretaceous granites (120–145 Ma). It shows that  $fO_2$  gradually decreased from Jurassic to Cretaceous (Figure 9).

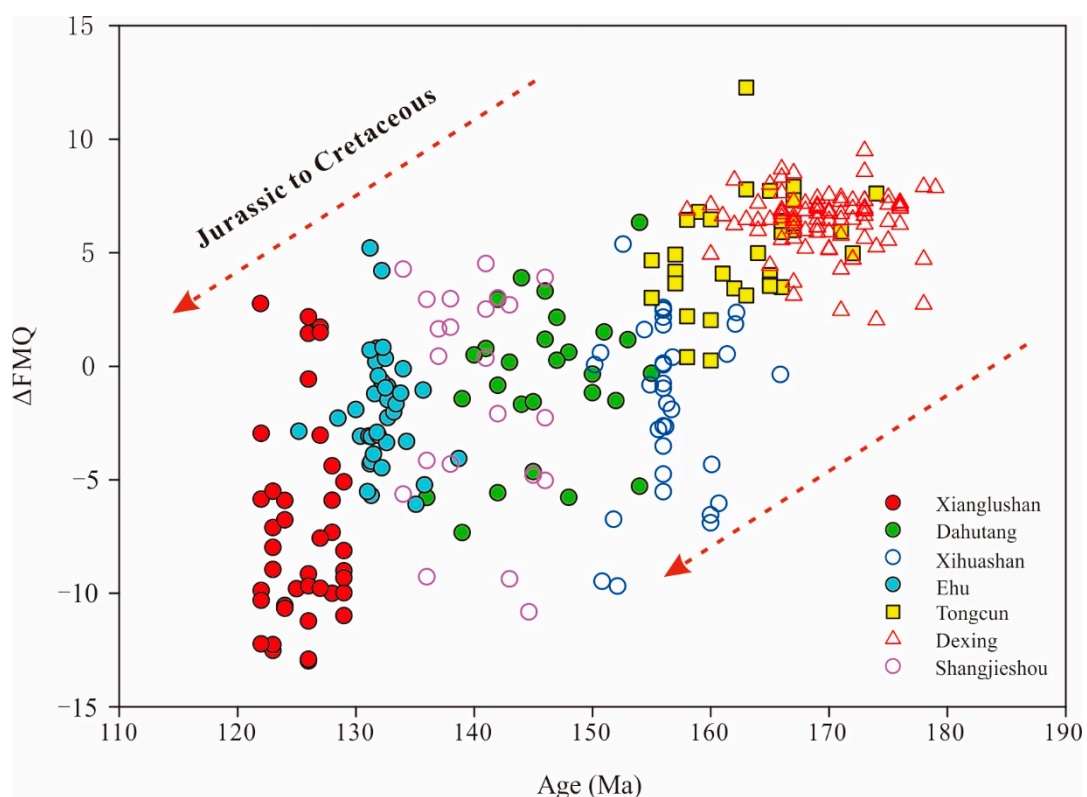


**Figure 9.**  $\log fO_2$  values vs. U-Pb age plot for the Yanshanian granites in Jiangxi Province ( $P < 0.01$  and  $R = 0.72$ ).

**Table 4.** Statistics of oxygen fugacity data for Yanshanian granites in Jiangxi Province.

Sample	n	FMQ		
Value		Mean	Min	Max
Late Jurassic	171	$3.54 \pm 4.02$	-10.29	11.87
Early Cretaceous	112	$-3.69 \pm 4.70$	-13	5.55

#### 5.4. Tectonic Implications

Although the origin of strong oxidation has been still argued, a broad consensus has been reached that high oxidization is associated with subduction zone [18,36,40]. Sun et al. [18,59] proposed that

subduction zone can release fluids to elevate oxygen fugacity. The closer distances from subduction zone are, the more fluids contribute and the higher oxygen fugacities are. For example, many hydrous (3–5 wt % water) arc magmas have high  $fO_2$ , ranging from NNO + 1 to NNO + 3 [18,60]. This phenomenon likely because of high amounts of dehydration-released fluid containing a lot of oxidized materials (i.e.,  $Fe^{3+}$ ,  $Mn^{4+}$ ,  $S^{6+}$ , and  $C^{4+}$ ) in subduction zones [18,60]. Additionally, the tectonic evolution of South China in late Mesozoic remains controversial for a long time [7,25,59]. A variety of tectonic models have been presented to address the Late Mesozoic large-scale magmatism and mineralization in South China, with most models invoking subduction of the paleo-Pacific plate [2,4,62]. Based on the drifting direction of the Pacific plate before 125 Ma [18,59] and the age distribution of magmatic rocks and mineralization zonation in the Late Jurassic to the Early Cretaceous in southern China like that in the South America. Sun et al. [59] proposed that the paleo-Pacific plate was subducting from NE to SW during ca. 180–125 Ma, and from SE to NW after 125 Ma in South China. This model may explain the differences in oxygen fugacity between the Late Jurassic and the Early Cretaceous granites in South China. According to this model, the Late Jurassic granites (such as Dexing granodiorite porphyry) are input more oxidized materials from the subduction than that of Early Cretaceous (such as Xianglushan biotite granite). Hence, it is observed that  $fO_2$  of granites gradually decreased from Jurassic to Cretaceous (Figure 9). Furthermore, Dahutang granite is closer from subduction zone than that of Xihuashan granite and Dahutang granite has the higher oxygen fugacity than that of Xihuashan granite.

### 5.5. Implications for Zircon as an Indicator

Zircons are widely distributed in igneous rocks and have stable geochemical properties. They faithfully record the information of zircon crystallization (i.e.,  $fO_2$ ). Moreover, with the development of analytical technology, researchers have obtained a lot of REE (rare earth element) as well as zircon age data. Ce and Eu are variable valence elements, whose valence state are affected by the redox conditions of magma. Unlike  $Ce_N/Ce_N^*$ ,  $Eu_N/Eu_N^*$  in zircon is generally affected by the crystallization of plagioclase [18,40]. Hence, most researchers use Ce anomalies of zircon/melt distribution coefficients (Di) to estimate the oxygen fugacity. A series of oxygen fugacity barometers have been developed based on Ce anomalies to indicate the redox conditions of magma since 2002 [37,43,64]. However, these methods produced a wide range of  $Ce/Ce^*$  ( $fO_2$ ) values which vary by up to 3 orders of magnitude for a single rock in some studies [43]. In this study, all zircon  $Ce_N/Ce_N^*$  ratios from selected granites also show a wide range (Figures 6 and 7). The cause of this phenomenon has not been well understood [40,43]. One possibility is that some tiny inclusions (i.e., monazite, apatite, and titanite) frequently can be detected in zircon. Meanwhile, as shown in Figure 6, no matter which calculation method is used, the  $fO_2$  of the Xianglushan granite is always lower than that of the ore-barren Ehu granite. Therefore, it is suggested that zircon  $fO_2$  may be still used as an indicator to discriminate ore-bearing and barren granites in areas of W mineralization.

## 6. Conclusions

1. LA-ICP-MS zircon U-Pb dating of the Xianglushan biotite granite yielded an Early Cretaceous age ( $125 \pm 1$  Ma). Age compilation indicates that the magmatism and W-Cu-(Mo) mineralization in northern Jiangxi Province are characterized by being multiphase, while the magmatism and W mineralization in southern Jiangxi Province occurred mainly in the Middle to Late Jurassic (165–150 Ma).
2. The ore-related granites in northern Jiangxi Province have a younger TDM2 age and clearly higher  $\epsilon Hf(t)$  values than those in southern Jiangxi Province, which seem to indicate a major source difference between the northern and southern granitic magmas in Jiangxi Province.
3. Compared with the coeval ore-barren Ehu granites, the low  $fO_2$  of the ore-related Xianglushan granite may have caused the W enrichment and mineralization, whilst the high  $fO_2$  of the

Dahutang granite may have facilitated the coexistence of Cu and W mineralization. Zircon  $fO_2$  may be still used as an indicator to discriminate ore-bearing and barren granites in some cases.

4. Variation of oxygen fugacity among different granites may support a model that the Paleo-Pacific plate was subducting southwestwardly, as proposed in some previous studies.

**Author Contributions:** X.-Y.L. conceived and designed the experiments; X.-Y.L. and J.-R.Z. performed the experiments; J.-R.Z. and X.-Y.L. analyzed the data; X.-Y.L. wrote the paper, assisted by all other authors; and C.-K.L. revised the manuscript. All authors have read and agreed to the published version of the manuscript.

**Funding:** This research was funded by the NSFC-China (418030401 and 41802251) and the China Scholarship Council Fund (201406380063).

**Acknowledgments:** We are grateful to the L.-L. Yuan for assistance with the sampling, and H. Song for the fruitful discussion. We appreciate Wei Gao for helping with the LA-ICP-MS analyses.

**Conflicts of Interest:** The authors declare no conflict of interest.

## Appendix A

**Table A1.** Crystallization temperatures, Ce anomalies, and magma oxygen fugacity of zircon grains from the Xianglushan, Dahutang, and Xihuashan granites.

Spot No.	$\delta^{143}\text{Ce}$ <sup>a</sup>	$\delta^{144}\text{Ce}$ <sup>b</sup>	$\delta\text{Eu}$	T (°C)	Age (Ma)	$\log fO_2$ <sup>a</sup>	FMQ <sup>a</sup>	$\log fO_2$ <sup>b</sup>	FMQ <sup>b</sup>
<b>Xianglushan</b>									
1	3	3	0.09	694	129	-27.23	-9.29	-26.07	-8.14
2	2	2	0.08	710	126	-27.69	-10.22	-26.62	-9.16
3	3	4	0.09	696	128	-26.38	-8.51	-25.21	-7.33
4	4	7	0.08	676	124	-26.82	-8.36	-24.39	-5.93
5	2	2	0.10	676	128	-29.28	-10.83	-28.48	-10.02
6	21	50	0.16	675	126	-20.36	-1.88	-17.04	1.44
7	4	4	0.11	681	127	-26.09	-7.76	-25.91	-7.59
8	4	10	0.09	736	122	-22.92	-6.15	-19.74	-2.97
9	15	45	0.12	719	126	-19.27	-2.04	-15.06	2.17
10	2	3	0.07	719	123	-26.27	-9.05	-25.21	-7.99
11	43	89	0.09	675	122	-17.60	0.88	-14.87	3.62
12	2	4	0.08	718	123	-26.20	-8.94	-24.37	-7.12
13	1	2	0.07	666	129	-30.79	-12.01	-29.78	-11.00
14	3	3	0.08	672	129	-28.37	-9.78	-27.62	-9.03
15	4	6	0.08	693	122	-25.88	-7.92	-23.84	-5.87
16	13	48	0.12	692	127	-21.08	-3.08	-16.28	1.71
17	5	8	0.10	684	129	-25.55	-7.34	-23.33	-5.11
18	2	1	0.09	728	124	-27.27	-10.30	-27.52	-10.55
19	2	3	0.11	786	124	-23.41	-7.93	-22.25	-6.78
20	5	7	0.10	682	123	-25.60	-7.31	-23.81	-5.52
21	2	2	0.05	674	124	-29.96	-11.45	-29.19	-10.68
22	1	1	0.10	703	123	-28.87	-11.20	-30.20	-12.53
23	2	2	0.10	704	122	-27.56	-9.93	-27.52	-9.89
24	1	1	0.09	712	123	-28.88	-11.48	-29.69	-12.28
25	2	2	0.10	688	122	-28.42	-10.31	-28.44	-10.32
26	1	1	0.15	714	122	-28.11	-10.75	-29.59	-12.24
27	1	1	0.10	685	126	-29.69	-11.50	-31.19	-13.00
28	2	2	0.07	707	125	-27.84	-10.29	-27.37	-9.81
29	2	2	0.10	741	123	-25.60	-8.97	-25.60	-8.97
30	2	2	0.08	655	126	-30.37	-11.24	-30.37	-11.24
31	9	16	0.08	765	126	-18.75	-2.75	-16.58	-0.58
32	3	3	0.06	655	126	-28.79	-9.69	-28.79	-9.69
33	2	1	0.08	688	126	-28.42	-10.32	-31.03	-12.92
34	56	7	0.09	793	127	-10.55	4.76	-18.38	-3.06
35	2	2	0.11	708	127	-27.33	-9.80	-27.33	-9.80

**Table A1.** *Cont.*

Spot No.	$\delta\text{Ce}^{\text{a}}$	$\delta\text{Ce}^{\text{b}}$	$\delta\text{Eu}$	T (°C)	Age (Ma)	$\log f\text{O}_2^{\text{a}}$	$\text{FMQ}^{\text{a}}$	$\log f\text{O}_2^{\text{b}}$	$\text{FMQ}^{\text{b}}$
36	13	39	0.08	712	127	-20.08	-2.65	-15.94	1.48
37	2	4	0.06	760	128	-24.66	-8.53	-22.05	-5.92
38	7	10	0.11	683	128	-24.01	-5.74	-22.67	-4.40
39	2	2	0.11	700	129	-27.73	-9.99	-27.73	-9.99
40	2	2	0.11	726	129	-26.35	-9.33	-26.35	-9.33
<b>Dahutang</b>									
D27-10	26	41	0.31	762	142	-14.94	1.13	-13.13	2.94
D27-11	27	16	0.33	841	151	-11.21	3.00	-13.11	1.10
D27-12	55	43	0.32	770	146	-11.65	4.21	-12.56	3.30
D27-17	4	5	0.09	731	142	-23.42	-6.55	-22.46	-5.59
D27-20	45	29	0.46	719	148	-15.01	2.21	-16.61	0.61
D27-21	9	13	0.08	746	144	-19.51	-3.03	-18.18	-1.69
D27-23	13	13	0.27	758	150	-17.59	-1.41	-17.77	-1.58
D27-24	12	14	0.38	746	145	-18.45	-1.98	-18.06	-1.58
D27-27	30	20	0.30	790	141	-13.02	2.37	-14.62	0.77
D27-32	19	13	0.33	793	150	-14.64	0.67	-16.07	-0.75
D27-33	3	3	0.10	723	139	-25.43	-8.31	-24.45	-7.34
D27-34	15	9	0.25	807	152	-14.93	0.04	-16.89	-1.93
D27-38	61	26	0.37	736	140	-12.98	3.78	-16.27	0.49
D27-44	9	3	0.14	794	136	-17.56	-2.29	-21.08	-5.80
D32-1	25	22	0.37	744	143	-16.00	0.54	-16.37	0.17
D32-21	20	24	0.10	816	147	-13.29	1.47	-12.62	2.14
D32-24	11	11	0.14	789	139	-16.72	-1.31	-16.86	-1.44
D32-25	2	4	0.05	759	148	-25.50	-9.34	-21.94	-5.79
D32-34	10	7	0.10	720	145	-20.44	-3.26	-21.84	-4.66
D32-35	59	55	0.22	757	144	-12.06	4.13	-12.30	3.89
D32-41	75	102	0.48	745	154	-11.75	4.76	-10.58	5.93
D32-43	25	23	0.25	739	147	-16.20	0.46	-16.42	0.25
D32-48	28	24	0.26	774	146	-14.05	1.71	-14.58	1.18
D32-58	9	21	0.23	775	153	-18.30	-2.57	-14.98	0.76
D32-60	13	16	0.43	755	142	-17.83	-1.57	-17.11	-0.85
D32-61	9	3	0.16	848	154	-15.15	-1.11	-19.34	-5.30
D32-62	50	22	0.56	709	155	-15.16	2.34	-18.22	-0.72
<b>Xihuashan</b>									
XHS-19-1C	29	9	0.23	744	155.6	-15.33	1.22	-19.75	-3.20
XHS-19-1R	2	4	0.15	737	160.7	-25.01	-8.30	-22.77	-6.05
XHS-19-2C	19	25	0.11	769	154.4	-15.73	0.17	-14.70	1.20
XHS-19-2R	54	90	0.16	724	152.6	-14.07	3.00	-12.10	4.97
XHS-19-3C	2	2	0.11	669	152.8	-30.37	-11.69	-28.97	-10.29
XHS-19-3R	12	37	0.17	739	162.2	-18.85	-2.17	-14.72	1.96
XHS-19-4C	2	3	0.13	757	160	-24.98	-8.78	-22.76	-6.56
XHS-19-4R	6	8	0.06	711	160.1	-22.92	-5.47	-21.80	-4.34
XHS-19-5C	18	8	0.29	774	156.2	-15.61	0.16	-18.84	-3.07
XHS-19-5R	2	4	0.14	701	160.8	-26.98	-9.25	-25.40	-7.67
XHS-19-7	22	36	0.21	720	162.1	-17.56	-0.37	-15.74	1.45
XHS-19-8R	6	5	0.04	701	151.8	-23.55	-5.84	-24.47	-6.76
XHS-19-9C	38	27	0.24	695	150.2	-16.96	0.94	-18.25	-0.34
XHS-19-11C	7	10	0.17	762	156.7	-19.78	-3.71	-18.39	-2.32
XHS-19-12R	5	13	0.18	738	156.3	-22.67	-5.96	-18.76	-2.05
XHS-19-13	4	9	0.07	890	156.8	-16.08	-2.90	-13.19	-0.01
XHS-19-14	21	14	0.33	780	165.9	-14.92	0.71	-16.40	-0.77
XHS-19-15C	77	35	0.18	678	150.7	-15.25	3.15	-18.21	0.19
XHS-19-15R	63	29	0.26	700	161.4	-14.71	3.03	-17.61	0.13
XHS-19-16	2	2	0.13	709	151.5	-28.07	-10.58	-27.58	-10.08
XHS-21-1R	4	9	0.15	829	154.9	-18.66	-4.18	-15.71	-1.23
XHS-21-2R	2	3	0.07	800	156	-22.60	-7.46	-20.68	-5.54

**Table A1.** *Cont.*

Spot No.	$\delta\text{Ce}^{\text{a}}$	$\delta\text{Ce}^{\text{b}}$	$\delta\text{Eu}$	T (°C)	Age (Ma)	$\log f\text{O}_2^{\text{a}}$	$\text{FMQ}^{\text{a}}$	$\log f\text{O}_2^{\text{b}}$	$\text{FMQ}^{\text{b}}$
XHS-21-3C	11	18	0.10	755	156	-18.31	-2.06	-16.52	-0.28
XHS-21-3R	4	9	0.08	680	156	-25.88	-7.54	-23.11	-4.77
XHS-21-4C	13	29	0.05	655	156	-23.18	-4.06	-20.28	-1.17
XHS-21-4R	12	14	0.10	684	156	-22.04	-3.83	-21.27	-3.05
XHS-21-5C	38	27	0.28	694	156	-17.05	0.89	-18.28	-0.35
XHS-21-5R	57	56	0.06	687	156	-15.86	2.27	-15.96	2.18
XHS-21-6C	18	63	0.04	667	156	-21.40	-2.64	-16.67	2.08
XHS-21-6R	34	69	0.10	654	156	-19.75	-0.61	-17.08	2.07
XHS-21-7C	9	12	0.26	779	156	-17.91	-2.27	-17.01	-1.38
XHS-21-8R	4	10	0.06	715	156	-24.19	-6.87	-20.85	-3.53
XHS-21-9C	50	33	0.19	748	156	-13.11	3.33	-14.69	1.75
XHS-21-9R	47	35	0.21	723	156	-14.67	2.45	-15.70	1.41
<b>Ehu</b>									
D019-07	25	22	0.05	769	131.8	-14.68	1.22	-15.10	0.79
D019-10	21	9	0.06	782	132.7	-14.80	0.78	-17.85	-2.28
D019-11	30	19	0.05	774	131.7	-13.76	2.02	-15.60	0.19
D019-14	24	11	0.03	768	133.2	-14.86	1.06	-17.94	-2.03
D019-15	7	10	0.02	830	132.7	-16.59	-2.14	-15.33	-0.89
D019-17	24	15	0.04	752	131.6	-15.63	0.71	-17.56	-1.22
D019-18	25	7	0.08	790	130.4	-13.70	1.67	-18.47	-3.10
D019-19	b.d.	10	0.03	724	134.3	b.d.	b.d.	-20.41	-3.33
D019-20	15	8	0.07	772	131.1	-16.61	-0.78	-18.91	-3.09
D019-21	b.d.	14	0.03	754	133.5	b.d.	b.d.	-17.51	-1.22
D019-22	b.d.	20	0.06	770	132.5	b.d.	b.d.	-15.53	0.34
D019-23	39	16	0.07	763	132.2	-13.30	2.75	-16.72	-0.67
D019-24	10	17	0.05	759	131.9	-18.77	-2.62	-16.58	-0.43
D019-33	b.d.	12	0.03	701	131.3	b.d.	b.d.	-20.83	-3.12
D019-34	17	9	0.03	745	131.9	-17.36	-0.84	-19.58	-3.06
D019-35	20	15	0.03	741	132.7	-17.00	-0.39	-18.10	-1.48
D019-41	6	21	0.04	743	134	-21.52	-4.95	-16.70	-0.12
D019-43	b.d.	22	0.04	772	131.2	b.d.	b.d.	-15.13	0.70
D019-44	2	5	0.04	744	131.3	-25.01	-8.47	-22.25	-5.71
D019-45	b.d.	14	0.04	740	133.4	b.d.	b.d.	-18.31	-1.68
D019-46	2	8	0.04	724	131.2	-26.23	-9.14	-21.41	-4.32
D019-47	1	4	0.05	834	131.3	-22.56	-8.20	-18.56	-4.21
D019-48	b.d.	13	0.02	739	130	b.d.	b.d.	-18.59	-1.92
D019-49	b.d.	24	0.02	758	132.3	b.d.	b.d.	-15.36	0.82
D019-50	20	7	0.07	731	132.2	-17.49	-0.60	-21.38	-4.49
D019-51	7	5	0.06	739	131	-21.14	-4.48	-22.20	-5.54
D019-55	b.d.	12	0.04	690	132.6	b.d.	b.d.	-21.42	-3.38
D019-60	11	4	0.04	792	135.8	-16.72	-1.39	-20.58	-5.24
D019-62	3	7	0.06	745	138.7	-24.26	-7.75	-20.59	-4.08
D019-63	2	8	0.05	777	131.8	-23.22	-7.53	-18.63	-2.93
D019-83	27	18	0.05	726	135.7	-16.61	0.43	-18.10	-1.06
D019-86	3	6	0.03	771	131.5	-22.23	-6.39	-19.73	-3.89
D019-87	5	6	0.06	823	125.2	-18.37	-3.76	-17.49	-2.88
D019-91	8	9	0.04	789	128.5	-17.86	-2.47	-17.70	-2.30
D019-92	203	118	0.04	708	131.2	-9.95	7.59	-11.99	5.55
D019-93	b.d.	95	0.02	688	132.2	b.d.	b.d.	-13.90	4.20
D019-97	b.d.	16	0.06	735	133.8	b.d.	b.d.	-17.97	-1.19
D019-102	b.d.	13	0.05	786	132.5	b.d.	b.d.	-16.43	-0.96
D019-111	1	3	0.03	782	135.1	-25.69	-10.13	-21.66	-6.10
Tongcun									
CB-13-6-01	95	61		735	157	-11.34	5.44	-13.01	3.77
CB-13-6-02	80	243		640	159	-17.37	2.22	-13.20	6.40
CB-13-6-06	76	142		615	165	-19.17	1.26	-16.82	3.62
CB-13-6-16	51	254		623	158	-20.15	0.01	-14.11	6.05
CB-13-6-18	33	24		721	160	-16.09	1.07	-17.30	-0.14

**Table A1.** *Cont.*

Spot No.	$\delta\text{Ce}^{\text{a}}$	$\delta\text{Ce}^{\text{b}}$	$\delta\text{Eu}$	T (°C)	Age (Ma)	$\log f\text{O}_2^{\text{a}}$	$\text{FMQ}^{\text{a}}$	$\log f\text{O}_2^{\text{b}}$	$\text{FMQ}^{\text{b}}$
CB-13-6-19	25	31		686	158	-19.02	-0.86	-18.16	0.01
CB-13-6-20	88	52		715	155	-12.68	4.65	-14.71	2.62
CB-13-6-29	34	245		613	167	-22.33	-1.82	-14.90	5.60
CB-13-6-30	44	25		790	160	-11.55	3.83	-13.75	1.63
TC-P1-5-02	69	84		720	164	-13.37	3.82	-12.60	4.59
TC-P1-5-03	50	166		599	161	-21.80	-0.79	-17.32	3.68
TC-P1-5-04	47	157		634	172	-19.73	0.06	-15.21	4.58
TC-P1-5-06	37	173		612	155	-22.05	-1.51	-16.27	4.27
TC-P1-5-07	50	115		781	174	-11.53	4.07	-8.39	7.21
TC-P1-5-12	45	218		624	166	-20.53	-0.40	-14.62	5.51
TC-P1-5-14	55	132		654	157	-17.93	1.21	-14.63	4.52
TC-P1-5-16	65	72		682	162	-15.64	2.64	-15.25	3.03
TC-P1-5-20	80	50		746	157	-11.45	5.04	-13.24	3.25
TC-P1-5-21	116	233		632	166	-16.49	3.37	-13.86	6.00
TC-P1-5-23	91	239		631	160	-17.48	2.42	-13.83	6.07
TC-P1-5-24	152	413		611	167	-16.83	3.75	-13.07	7.51
TC-P1-5-27	47	88		615	158	-20.95	-0.51	-18.64	1.80
TC-P1-29-01	28	117		610	163	-23.28	-2.67	-17.89	2.72
TC-P1-29-04	88	281		655	163	-16.11	3.00	-11.73	7.39
TC-P1-29-07	67	75		684	165	-15.43	2.80	-15.02	3.21
TC-P1-29-13	106	1083		635	163	-16.63	3.14	-7.88	11.88
TC-P1-29-15	27	80		670	166	-19.62	-0.97	-15.55	3.09
TC-P1-29-16	46	117		623	165	-20.57	-0.41	-17.02	3.14
TC-P1-29-17	93	218		637	167	-16.98	2.71	-13.80	5.90
TC-P1-29-20	22	241		613	171	-23.89	-3.39	-14.97	5.54
TC-P1-29-27	38	222		670	167	-18.41	0.23	-11.73	6.92
TC-P1-29-29	57	321		636	165	-18.90	0.83	-12.40	7.33
Dexing									
FJW1-37-1	228	181		682	166	-10.95	7.34	-11.83	6.47
FJW1-37-2.1	101	66		644	174	-16.23	3.22	-17.81	1.64
FJW1-37-2	82	119		678	168	-15.00	3.39	-13.59	4.80
FJW1-37-2.2	b.d.	204		669	169	b.d.	b.d.	-12.11	6.57
FJW1-37-3	280	195		671	170	-10.81	7.81	-12.17	6.45
FJW1-37-4	92	79		679	167	-14.52	3.86	-15.08	3.30
FJW1-37-5	347	167		670	173	-10.02	8.61	-12.78	5.86
FJW1-37-7	b.d.	221		665	164	b.d.	b.d.	-12.01	6.78
FJW1-37-8	64	91		687	165	-15.41	2.71	-14.09	4.04
FJW1-37-11	126	155		676	169	-13.53	4.94	-12.74	5.73
FJW1-37-12	91	197		669	168	-15.13	3.54	-12.21	6.45
FJW1-37-13	290	175		657	167	-11.47	7.57	-13.37	5.67
FJW1-37-14	b.d.	192		668	171	b.d.	b.d.	-12.40	6.32
FJW1-37-15	b.d.	207		664	166	b.d.	b.d.	-12.35	6.48
FJW1-37-16	269	249		652	167	-12.05	7.15	-12.34	6.86
FJW1-37-17	223	156		690	166	-10.53	7.50	-11.89	6.14
FJW1-37-2.3	b.d.	150		693	165	b.d.	b.d.	-11.90	6.06
FJW1-37-2.4	b.d.	251		665	166	b.d.	b.d.	-11.57	7.24
FJW1-37-2.5	b.d.	164		681	169	b.d.	b.d.	-12.24	6.08
FJW1-37-2.6	b.d.	173		683	169	b.d.	b.d.	-11.89	6.35
FJW1-37-2.8	328	184		678	166	-9.77	8.62	-11.95	6.44
FJW1-37-2.9	b.d.	156		670	164	b.d.	b.d.	-13.07	5.58
FJW1-37-2.10	399	252		677	165	-9.09	9.34	-10.81	7.61
FJW1-37-2.11	100	150		662	173	-15.18	3.70	-13.66	5.23
FJW1-37-2.12	b.d.	149		676	168	b.d.	b.d.	-12.91	5.57
FJW1-37-2.13	217	289		684	166	-11.00	7.22	-9.93	8.29
FJW1-37-2.14	384	224		677	170	-9.28	9.16	-11.30	7.14
FJW1-37-2.15	145	152		670	169	-13.34	5.32	-13.16	5.50
FJW1-37-2.16	78	158		685	163	-14.80	3.39	-12.13	6.06

**Table A1.** *Cont.*

Spot No.	$\delta\text{Ce}^{\text{a}}$	$\delta\text{Ce}^{\text{b}}$	$\delta\text{Eu}$	T (°C)	Age (Ma)	$\log f\text{O}_2^{\text{a}}$	$\text{FMQ}^{\text{a}}$	$\log f\text{O}_2^{\text{b}}$	$\text{FMQ}^{\text{b}}$
TC44-1	180	107		690	170	-11.37	6.67	-13.31	4.73
TC44-4	b.d.	63		676	178	b.d.	b.d.	-16.13	2.34
TC44-6	221	96		674	171	-11.48	7.03	-14.62	3.88
TC3-1	150	143		710	170	-10.94	6.53	-11.12	6.35
TC3-2	86	94		701	160	-13.54	4.19	-13.19	4.54
TC3-3	81	121		674	170	-15.26	3.25	-13.74	4.77
TC3-4	28	125		812	173	-12.27	2.60	-6.69	8.18
TC3-5	260	112		669	172	-11.18	7.50	-14.36	4.32
TC3-6	33	63		665	171	-19.15	-0.36	-16.73	2.06
TC43-1	259	184		657	176	-11.90	7.14	-13.19	5.85
TC43-2	265	274		684	167	-10.24	7.98	-10.11	8.11
TC43-3	322	162		700	176	-8.59	9.15	-11.18	6.56
TC43-4	362	192		690	173	-8.76	9.30	-11.16	6.90
TC44-8	431	186		661	170	-9.74	9.18	-12.90	6.02
TC44-9	b.d.	179		657	169	b.d.	b.d.	-13.32	5.74
TC44-10	b.d.	177		686	173	b.d.	b.d.	-11.68	6.49
TC44-13	b.d.	213		627	170	b.d.	b.d.	-14.49	5.52
TC44-14	b.d.	207		658	166	b.d.	b.d.	-12.69	6.32
TC44-15	330	211		670	175	-10.22	8.42	-11.90	6.74
TC44-16	240	201		659	173	-12.05	6.92	-12.72	6.25
TC44-17	b.d.	106		677	178	b.d.	b.d.	-14.13	4.31
TC44-19	206	175		666	167	-12.25	6.53	-12.87	5.91
TC3-9	354	165		655	171	-10.85	8.26	-13.74	5.37
TC3-10	b.d.	225		672	171	b.d.	b.d.	-11.56	7.03
TC3-12	392	198		676	176	-9.24	9.23	-11.81	6.66
TC3-13	264	346		688	173	-10.03	8.07	-9.00	9.09
TC3-14	397	180		665	175	-9.85	8.96	-12.83	5.98
TC3-15	b.d.	226		659	169	b.d.	b.d.	-12.31	6.68
TC3-16	422	252		685	162	-8.46	9.74	-10.40	7.80
TC3-17	357	192		674	158	-9.72	8.81	-12.05	6.48
TC3-18	43	110		671	172	-17.82	0.79	-14.28	4.32
TC3-19	b.d.	184		691	168	b.d.	b.d.	-11.25	6.77
TC3-20	243	204		674	160	-11.17	7.37	-11.83	6.71
TC3-21	175	210		667	169	-12.80	5.94	-12.11	6.63
TC3-22	383	164		680	172	-9.07	9.26	-12.26	6.07
TC3-23	258	179		666	164	-11.37	7.39	-12.75	6.01
TC3-24	371	171		666	162	-10.02	8.75	-12.94	5.83
TC3-25	b.d.	126		686	167	b.d.	b.d.	-12.92	5.24
TC3-26	429	151		698	161	-7.66	10.16	-11.59	6.22
TC3-27	389	142		668	166	-9.73	8.98	-13.53	5.18
TC3-28	b.d.	290		654	179	b.d.	b.d.	-11.68	7.47
TC3-29	230	67		681	167	-10.93	7.38	-15.58	2.73
TC3-30	439	251		674	178	-8.90	9.61	-11.00	7.51
TC3-32	30	124		685	175	-18.42	-0.23	-13.04	5.15
TC3-33	b.d.	221		673	169	b.d.	b.d.	-11.56	6.99
TC3-34	386	201		683	172	-8.87	9.37	-11.33	6.91
TC43-6	391	194		687	173	-8.60	9.53	-11.23	6.90
TC43-7	314	138		660	174	-10.99	7.96	-14.09	4.86
TC43-8	b.d.	178		688	173	b.d.	b.d.	-11.53	6.57
TC43-9	b.d.	162		697	173	b.d.	b.d.	-11.40	6.45
TC43-10	b.d.	192		658	167	b.d.	b.d.	-13.01	6.03
TC43-11	b.d.	182		702	175	b.d.	b.d.	-10.66	7.04
TC43-12	b.d.	240		657	171	b.d.	b.d.	-12.19	6.86
TC43-13	333	268		680	166	-9.62	8.72	-10.42	7.92
TC43-14	b.d.	239		657	176	b.d.	b.d.	-12.24	6.82
TC43-15	293	180		672	167	-10.54	8.03	-12.38	6.19
TC43-16	303	156		686	171	-9.61	8.54	-12.10	6.05
TC43-17	b.d.	228		653	172	b.d.	b.d.	-12.65	6.54
TC43-20	b.d.	199		680	176	b.d.	b.d.	-11.59	6.77

**Table A1.** Cont.

Spot No.	$\delta\text{Ce}^{\text{a}}$	$\delta\text{Ce}^{\text{b}}$	$\delta\text{Eu}$	T (°C)	Age (Ma)	$\log f\text{O}_2^{\text{a}}$	$\text{FMQ}^{\text{a}}$	$\log f\text{O}_2^{\text{b}}$	$\text{FMQ}^{\text{b}}$
Shangjieshou									
CB-7-1-02	6	9		651	134	-26.75	-7.51	-24.89	-5.65
CB-7-1-03	23	87		702	134	-18.42	-0.73	-13.43	4.27
CB-7-1-04	11	10		682	138	-22.40	-4.12	-22.61	-4.33
CB-7-1-07	17	51		730	136	-18.16	-1.24	-13.98	2.94
CB-7-1-08	22	84		644	141	-22.00	-2.53	-16.96	2.51
CB-7-1-09	25	94		644	138	-21.51	-2.04	-16.50	2.96
CB-7-1-10	20	63		651	137	-22.01	-2.76	-17.61	1.63
CB-7-1-11	6	3		656	143	-25.97	-6.89	-28.47	-9.38
CB-7-1-12	22	80		701	146	-18.65	-0.93	-13.82	3.90
CB-7-1-15	5	2		645	145	-27.43	-7.99	-30.89	-11.46
CB-7-1-16	27	129		657	141	-20.41	-1.36	-14.54	4.51
CB-7-1-17	11	19		680	142	-22.53	-4.19	-20.45	-2.11
CB-7-1-18	7	3		675	136	-24.53	-6.04	-27.78	-9.29
CB-7-1-19	15	29		716	137	-19.19	-1.90	-16.87	0.43
CB-7-1-20	11	13		658	136	-23.80	-4.79	-23.19	-4.17
CB-7-1-21	11	10		659	146	-23.83	-4.85	-24.04	-5.05
CB-7-1-22	18	51		682	138	-20.43	-2.15	-16.57	1.71
CB-7-1-23	11	11		655	145	-23.86	-4.75	-23.92	-4.81
CB-7-1-24	17	50		721	143	-18.55	-1.38	-14.47	2.69
CB-7-1-25	10	31		701	141	-21.68	-3.96	-17.38	0.35
CB-7-1-26	6	16		694	146	-24.15	-6.23	-20.22	-2.29
CB-7-1-27	21	61		704	142	-18.71	-1.08	-14.64	3.00

Notes: (1) Temperatures were calculated with the Ti-in-zircon thermometer [37]. (2) Oxygen fugacities were calculated by the method proposed by [43]. (3) Trace elements data from [5] for Dahutang complex, Qiu et al. [26] for Ehu granite and Yang et al. [28] for Xihuashan granite. b.d. = below the detection limit. "a" and "b" mean the values are calculated by the La-Pr and Nd-Sm interpolation methods respectively.

**Table A2.** Zircon Hf isotope data of the Dahutang and Xihuashan granites.

Spot	$^{176}\text{Yb}/^{177}\text{Hf}$	$^{176}\text{Lu}/^{177}\text{Hf}$	$^{176}\text{Hf}/^{177}\text{Hf}$	$\varepsilon\text{Hf(t)}$	TDM2(Ma)
Dahutang					
1	0.0029405	0.0000436	0.2824949	-6.5	1042
2	0.0118261	0.0002274	0.2824995	-6.4	1078
3	0.0069998	0.0001264	0.2825899	-3.1	1143
4	0.0250298	0.0005874	0.2825216	-5.6	1166
5	0.0182471	0.0003612	0.2824659	-7.6	1194
6	0.0328127	0.0006971	0.2825122	-5.9	1195
7	0.0013712	0.0000202	0.2824347	-8.6	1210
8	0.0056955	0.0000978	0.2825509	-4.5	1219
9	0.0160187	0.0003447	0.2824923	-6.6	1229
10	0.0205019	0.0004278	0.2824932	-6.6	1236
11	0.0593198	0.0012226	0.2826147	-2.4	1241
12	0.0240443	0.0004526	0.2825063	-6.1	1242
13	0.0373943	0.0008386	0.2824021	-10	1250
14	0.0358791	0.0008128	0.2825389	-5.2	1286
15	0.0435529	0.0008814	0.2824529	-8.2	1310
16	0.0209965	0.0004417	0.2824873	-7	1336
17	0.0240384	0.0004984	0.282521	-5.8	1394
Xihuashan					
XHS-19-1	0.02924	0.00102	0.282296	-13.5	1473
XHS-19-2	0.01224	0.00045	0.282298	-13.4	1475
XHS-19-3	0.06476	0.00209	0.28231	-13.1	1480
XHS-19-4	0.03147	0.00108	0.282346	-11.7	1481
XHS-19-5	0.03242	0.00121	0.282274	-14.3	1482
XHS-19-6	0.02409	0.00085	0.282323	-12.5	1487

**Table A2.** *Cont.*

Spot	$^{176}\text{Yb}/^{177}\text{Hf}$	$^{176}\text{Lu}/^{177}\text{Hf}$	$^{176}\text{Hf}/^{177}\text{Hf}$	$\varepsilon\text{Hf(t)}$	TDM2(Ma)
XHS-19-7	0.02377	0.00084	0.282271	-14.3	1488
XHS-19-9	0.02463	0.00087	0.282345	-11.7	1490
XHS-19-10	0.05415	0.00187	0.282352	-11.6	1490
XHS-19-11	0.03011	0.001	0.282257	-14.9	1498
XHS-19-13	0.03034	0.00106	0.282333	-12.2	1501
XHS-19-14	0.03688	0.00137	0.28234	-12	1502
XHS-19-16	0.04093	0.00155	0.282306	-13.2	1504
XHS-19-17	0.03498	0.00118	0.282287	-13.8	1505
XHS-19-18	0.03031	0.00106	0.282306	-13.1	1509
XHS-19-19	0.02442	0.0009	0.282344	-11.8	1512
XHS-19-20	0.02868	0.00107	0.282349	-11.6	1515
XHS-9-8	0.13465	0.00438	0.282339	-12.3	1520
XHS-9-10	0.05669	0.00197	0.282323	-12.6	1524
XHS-9-15	0.13349	0.00445	0.28232	-13	1530
XHS-9-17	0.07194	0.00274	0.282331	-12.4	1547
XHS-9-18	0.07813	0.00286	0.282343	-12	1552
XHS-9-19	0.04143	0.00151	0.282356	-11.4	1553
XHS-9-20	0.21745	0.00776	0.282351	-12.2	1556
XHS-10-4	0.02976	0.00103	0.282353	-11.5	1564
XHS-10-5	0.12769	0.00443	0.282347	-12	1570
XHS-10-6	0.02777	0.00105	0.282335	-12.1	1585
XHS-10-10	0.10121	0.00369	0.282358	-11.6	1607
XHS-10-18	0.07579	0.00283	0.282341	-12.1	1610
XHS-10-19	0.13134	0.00474	0.282355	-11.8	1634

## References

- Feng, C.Y.; Zeng, Z.L.; Zhang, D.Q.; Qu, W.J.; Du, A.D.; Li, D.X.; She, H.Q. SHRIMP zircon U–Pb and molybdenite Re–Os isotopic dating of the tungsten deposits in the Tianmenshan–Hongtaoling W–Sn orefield, southern Jiangxi Province, China, and geological implications. *Ore Geol. Rev.* **2011**, *43*, 8–25. [[CrossRef](#)]
- Feng, C.Y.; Zhao, Z.; Qu, W.J.; Zeng, Z.L. Temporal consistency between granite evolution and tungsten mineralization in Huamei’ao, southern Jiangxi Province, China: Evidence from precise zircon U–Pb, molybdenite Re–Os, and muscovite  $^{40}\text{Ar}$ – $^{39}\text{Ar}$  isotope geochronology. *Ore Geol. Rev.* **2015**, *65*, 1005–1020. [[CrossRef](#)]
- Zhang, Y.; Gao, J.F.; Ma, D.S.; Pan, J.Y. The role of hydrothermal alteration in tungsten mineralization at the Dahutang tungsten deposit, South China. *Ore Geol. Rev.* **2018**, *95*, 1008–1027. [[CrossRef](#)]
- Mao, J.W.; Xiong, B.K.; Liu, J.; Pirajno, F.; Cheng, Y.B.; Ye, H.S.; Song, S.W.; Dai, P. Molybdenite Re/Os dating, zircon U–Pb age and geochemistry of granitoids in the Yangchuling porphyry W–Mo deposit (Jiangnan tungsten ore belt), China: Implications for petrogenesis, mineralization and geodynamic setting. *Lithos* **2017**, *286–287*, 35–52. [[CrossRef](#)]
- Wei, W.; Lai, C.; Yan, B.; Zhu, X.; Song, S.; Liu, L. Petrogenesis and Metallogenic Implications of Neoproterozoic Granodiorite in the Super-Large Shimensi Tungsten-Copper Deposit in Northern Jiangxi, South China. *Minerals* **2018**, *8*, 429. [[CrossRef](#)]
- Wang, X.D.; Ni, P.; Yuan, S.D.; Wu, S.H. Fluid inclusion studies on coexisting cassiterite and quartz from the Piaotang tungsten deposit, Jiangxi Province, China. *Acta Geol. Sin.* **2013**, *87*, 850–859, (In Chinese with English Abstract).
- Yuan, S.D.; Peng, J.T.; Hu, R.Z.; Li, H.M.; Shen, N.P.; Zhang, D.L. A precise U–Pb age on cassiterite from the Xianghualing tin-polymetallic deposit (Hunan, South China). *Miner. Depos.* **2008**, *43*, 375–382. [[CrossRef](#)]
- Wei, W.F.; Shen, N.P.; Yan, B.; Lai, C.K.; Yang, J.H.; Gao, W.; Liang, F. Petrogenesis of ore-forming granites with implications for W-mineralization in the super-large Shimensi tungsten-dominated polymetallic deposit in northern Jiangxi Province, South China. *Ore Geol. Rev.* **2018**, *95*, 1123–1139. [[CrossRef](#)]
- Mao, Z.H.; Liu, J.J.; Mao, J.W.; Deng, J.; Zhang, F.; Meng, X.Y.; Xiong, B.K.; Xiang, X.K.; Luo, X.H. Geochronology and geochemistry of granitoids related to the giant Dahutang tungsten deposit, middle

- Yangtze River region, China: Implications for petrogenesis, geodynamic setting, and mineralization. *Gondwana Res.* **2015**, *28*, 816–836. [[CrossRef](#)]
- 10. Pan, X.F.; Hou, Z.Q.; Zhao, M.; Chen, G.H.; Rao, J.F.; Li, Y.; Wei, J.; Ouyang, Y.P. Geochronology and geochemistry of the granites from the Zhuxi W-Cu ore deposit in South China: Implication for petrogenesis, geodynamical setting and mineralization. *Lithos* **2018**, *304–307*, 155–179. [[CrossRef](#)]
  - 11. Zhang, H.; Ling, M.X.; Liu, Y.L.; Tu, X.L.; Wang, F.Y.; Li, C.Y.; Liang, H.Y.; Yang, X.Y.; Arndt, N.T.; Sun, W.D. High oxygen fugacity and slab melting linked to Cu mineralization: Evidence from Dexing porphyry copper deposits, southeastern China. *J. Geol.* **2013**, *121*, 289–305. [[CrossRef](#)]
  - 12. Zhang, C.C.; Sun, W.D.; Wang, J.T.; Zhang, L.P.; Sun, S.J.; Wu, K. Oxygen fugacity and porphyry mineralization: A zircon perspective of Dexing porphyry Cu deposit, China. *Geochim. Cosmochim. Acta* **2017**, *206*, 343–363. [[CrossRef](#)]
  - 13. Guo, C.L.; Chen, Y.C.; Zeng, Z.L.; Lou, F.S. Petrogenesis of the Xihuashan granites in southeastern China: Constraints from geochemistry and in-situ analyses of zircon U-Pb-Hf-O isotopes. *Lithos* **2012**, *148*, 209–227. [[CrossRef](#)]
  - 14. Gardiner, N.J.; Hawkesworth, C.J.; Robb, L.J.; Whitehouse, M.J.; Roberts, M.W.; Kirkland, C.L.; Evans, N.J. Contrasting Cu-Au and Sn-W granite metallogeny through the zircon record. *Trans. Inst. Min. Metall. Sect. B Appl. Earth Sci.* **2017**, *126*, 57. [[CrossRef](#)]
  - 15. Gilder, S.A.; Keller, G.R.; Luo, M.; Goodell, P. Eastern Asia and the western Pacific timing and spatial distribution of rifting in China. *Tectonophysics* **1991**, *197*, 225–243. [[CrossRef](#)]
  - 16. Zhou, X.M.; Li, W.X. Origin of Late Mesozoic igneous rocks in Southeastern China: Implications for lithosphere subduction and underplating of mafic magmas. *Tectonophysics* **2000**, *326*, 269–287. [[CrossRef](#)]
  - 17. Hu, R.Z.; Zhou, M.F. Multiple Mesozoic mineralization events in South China—An introduction to the thematic issue. *Miner. Depos.* **2012**, *47*, 579–588. [[CrossRef](#)]
  - 18. Li, X.Y.; Chi, G.X.; Zhou, Y.Z.; Deng, T.; Zhang, J.R. Oxygen fugacity of Yanshanian granites in South China and implications for metallogeny. *Ore Geol. Rev.* **2017**, *88*, 690–701. [[CrossRef](#)]
  - 19. Mao, J.W.; Chen, Y.B.; Chen, M.H.; Pirajno, F. Major types and time–space distribution of Mesozoic ore deposits in South China and their geodynamic settings. *Miner. Depos.* **2013**, *48*, 267–294.
  - 20. Mao, J.W.; Zhang, J.D.; Pirajno, F.; Ishiyama, D.; Su, H.; Guo, C.L.; Chen, Y.C. Porphyry Cu–Au–Mo and epithermal Ag–Pb–Zn–distal hydrothermal Au deposits in the Dexing area, Jiangxi province, East China—A linked ore system. *Ore Geol. Rev.* **2011**, *43*, 203–216. [[CrossRef](#)]
  - 21. Shu, X.J.; Wang, X.L.; Sun, T.; Xu, X.; Dai, M.N.; 2011. Trace elements, U–Pb ages and Hf isotopes of zircons from Mesozoic granites in the western Nanling Range, South China: Implications for petrogenesis and W–Sn mineralization. *Lithos* **2011**, *127*, 468–482. [[CrossRef](#)]
  - 22. Zhong, J.; Chen, Y.J.; Pirajno, F.; Chen, J.; Li, J.; Qi, J.P.; Li, N. Geology, geochronology, fluid inclusion and H–O isotope geochemistry of the Luoboling porphyry Cu–Mo deposit, Zijinshan Orefield, Fujian Province, China. *Ore Geol. Rev.* **2014**, *57*, 61–77. [[CrossRef](#)]
  - 23. Dai, P.; Mao, J.W.; Wu, S.H.; Xie, G.Q.; Luo, X.H. Multiple dating and tectonic setting of the Early Cretaceous Xianglushan W deposit, Jiangxi Province, South China. *Ore Geol. Rev.* **2018**, *95*, 1161–1178. [[CrossRef](#)]
  - 24. Wu, S.H.; Mao, J.W.; Ireland, T.R.; Zhao, Z.; Yao, Y.P.; Sun, W.D. Comparative geochemical study of scheelite from the Shizhuyuan and Xianglushan tungsten skarn deposits, South China: Implications for scheelite mineralization. *Ore Geol. Rev.* **2019**, *95*, 448–464. [[CrossRef](#)]
  - 25. Qiu, J.T.; Qiu, L. Geochronology and magma oxygen fugacity of Ehu S-type granitic pluton in Zhe-Gan-Wan region, SE China. *Geochemistry* **2014**, *3*, 441–448. [[CrossRef](#)]
  - 26. Sun, K.K.; Chen, B.; Deng, J.; Ma, X.H. Source of copper in the giant Shimensi W-Cu-Mo polymetallic deposit, South China: Constraints from chalcopyrite geochemistry and oxygen fugacity of ore-related granites. *Ore Geol. Rev.* **2018**, *101*, 919–935. [[CrossRef](#)]
  - 27. Yang, J.H.; Kang, L.F.; Peng, J.T.; Zhong, H.; Gao, J.F.; Liu, L. In-situ elemental and isotopic compositions of apatite and zircon from the Shuikoushan and Xihuashan granitic plutons: Implication for Jurassic granitoid-related Cu-Pb-Zn and W mineralization in the Nanling Range, South China. *Ore Geol. Rev.* **2018**, *93*, 382–403. [[CrossRef](#)]
  - 28. Zong, K.Q.; Klemd, R.; Yuan, Y.; He, Z.Y.; Guo, J.L.; Shi, X.L.; Liu, Y.S.; Hu, Z.C.; Zhang, Z.M. The assembly of Rodinia: The correlation of early Neoproterozoic (ca. 900 Ma) high-grade metamorphism and continental

- arc formation in the southern Beishan Orogen, southern Central Asian Orogenic Belt (CAOB). *Precambrian Res.* **2017**, *290*, 32–48. [[CrossRef](#)]
29. Hu, Z.C.; Zhang, W.; Liu, Y.S.; Gao, S.; Li, M.; Zong, K.Q.; Chen, H.H.; Hu, S.H. “Wave” signal smoothing and mercury removing device for laser ablation quadrupole and multiple collector ICP-MS analysis: Application to lead isotope analysis. *Anal. Chem.* **2015**, *87*, 1152–1157. [[CrossRef](#)]
30. Liu, Y.S.; Gao, S.; Hu, Z.C.; Gao, C.G.; Zong, K.Q.; Wang, D.B. Continental and oceanic crust recycling-induced melt-peridotite interactions in the Trans-North China Orogen: U-Pb dating, Hf isotopes and trace elements in zircons of mantle xenoliths. *J. Petrol.* **2010**, *51*, 537–571. [[CrossRef](#)]
31. Sláma, J.; Košler, J.; Condon, D.J.; Crowley, J.L.; Gerdes, A.; Hanchar, J.M.; Horstwood, M.S.A.; Morris, G.A.; Nasdala, L.; Norberg, N.; et al. Plešovice zircon—A new natural reference material for U-Pb and Hf isotopic microanalysis. *Chem. Geol.* **2008**, *249*, 1–35. [[CrossRef](#)]
32. Ludwig, K.R. *ISOPLOT 3.00: A Geochronological Toolkit for Microsoft Excel*; Berkeley Geochronology Center: Berkeley, CA, USA, 2003.
33. Woodhead, J.D.; Herdt, J.M.; Shelley, M.; Eggins, S.; Kemp, R. Zircon Hf-isotope analysis with an excimer laser, depth profiling, ablation of complex geometries, and concomitant age estimation. *Chem. Geol.* **2004**, *209*, 121–135. [[CrossRef](#)]
34. Fisher, C.M.; Vervoort, J.D.; Hanchar, J.M. Guidelines for reporting zircon Hf isotopic data by LA-MC-ICPMS and potential pitfalls in the interpretation of these data. *Chem. Geol.* **2014**, *363*, 125–133. [[CrossRef](#)]
35. Blichert-Toft, J.; Chauvel, C.; Albarede, F. Separation of Hf and Lu for high-precision isotope analysis of rock samples by magnetic sector-multiple collector ICP-MS. *Contrib. Mineral. Petrol.* **1997**, *127*, 248–260. [[CrossRef](#)]
36. Trail, D.; Watson, E.B.; Tailby, N.D. Ce and Eu anomalies in zircon as proxies for the oxidation state of magmas. *Geochim. Cosmochim. Acta* **2012**, *97*, 70–87. [[CrossRef](#)]
37. Ferry, J.M.; Watson, E.B. New thermodynamic models and revised calibrations for the Ti-in-zircon and Zr-in-rutile thermometers. *Contrib. Mineral. Petrol.* **2007**, *154*, 429–437. [[CrossRef](#)]
38. Meng, X.Y.; Mao, J.W.; Zhang, C.Q.; Zhang, D.Y.; Liu, H. Melt recharge,  $fO_2$ -T conditions, and metal fertility of felsic magmas: Zircon trace element chemistry of Cu-Au porphyries in the Sanjiang orogenic belt, southwest China. *Miner. Depos.* **2018**, *53*, 649–663. [[CrossRef](#)]
39. Anders, E.; Grevesse, N. Abundances of the elements: Meteoritic and solar. *Geochim. Cosmochim. Acta* **1989**, *53*, 197–214. [[CrossRef](#)]
40. Dilles, J.H.; Kent, A.J.; Wooden, J.L.; Tosdal, R.M.; Koleszar, A.; Lee, R.G.; Farmer, L.P. Zircon compositional evidence for sulfur-degassing from ore-forming arc magmas. *Econ. Geol.* **2015**, *110*, 241–251. [[CrossRef](#)]
41. Smythe, D.J.; Brenan, J.M. Magmatic oxygen fugacity estimated using zircon melt partitioning of cerium. *Earth Planet. Sci. Lett.* **2016**, *453*, 260–266. [[CrossRef](#)]
42. Zhang, J.R.; Li, X.Y.; Ye, M. Research progress on Ce anomaly method for calculating oxygen fugacity of granite and applicability. *Chin. Rare Earths* **2018**, *39*, 20–27, (In Chinese with English Abstract).
43. Loader, M.A.; Wilkinson, J.J.; Armstrong, R.N. The effect of titanite crystallization on Eu and Ce anomalies in zircon and its implications for the assessment of porphyry Cu deposit fertility. *Earth Planet. Sci. Lett.* **2017**, *472*, 107–119. [[CrossRef](#)]
44. Blichert-Toft, J.; Albarede, F. The Lu-Hf isotope geochemistry of chondrites and the evolution of the mantle–crust system. *Earth Planet. Sci. Lett.* **1997**, *148*, 243–258. [[CrossRef](#)]
45. Griffin, W.L.; Pearson, N.J.; Belousova, E.; Jackson, S.E.; van Achterbergh, E.; O'Reilly, S.Y.; Shee, S.R. The Hf isotope composition of cratonic mantle: LAM-MC-ICPMS analysis of zircon megacrysts in kimberlites. *Geochim. Cosmochim. Acta* **2000**, *64*, 133–147. [[CrossRef](#)]
46. Bea, F.; Montero, P.; Molina, J.F.; Scarrow, J.H.; Cambeses, A.; Moreno, J.A. Lu-Hf ratios of crustal rocks and their bearing on zircon Hf isotope model ages: The effects of accessories. *Chem. Geol.* **2018**, *484*, 179–190. [[CrossRef](#)]
47. Huang, L.C.; Jiang, S.Y. Highly fractionated S-type granites from the giant Dahutang tungsten deposit in Jiangnan Orogen, Southeast China: Geochronology, petrogenesis and their relationship with W-mineralization. *Lithos* **2014**, *202*, 207–226. [[CrossRef](#)]
48. Su, H.M.; Jiang, S.Y. A comparison study of tungsten-bearing granite and related mineralization in the northern Jiangxi-southern Anhui provinces and southern Jiangxi Province in South China. *Sci. China Earth Sci.* **2017**, *60*, 1942–1958. [[CrossRef](#)]

49. Xiang, X.G.; Liu, X.M.; Zhan, G.N. Discovery and prospecting significance of super large tungsten deposits in Shimensi mining area, Dahutang, Jiangxi Province. *Resour. Surv. Environ.* **2012**, *33*, 141–151, (In Chinese with English Abstract).
50. Wang, X.G.; Liu, Z.Q.; Liu, S.B.; Wang, C.H.; Liu, J.G.; Wang, H.Z.; Chen, G.H.; Zhang, S.D.; Liu, X.L. LA-ICP-MS Zircon U-Pb Dating and Geochemistry of Fine Granite from Zhuxi Copper-Tungsten Mine, Jiangxi Province. *Rock Miner. Test.* **2015**, *34*, 592–599, (In Chinese with English Abstract).
51. Chen, G.H.; Shu, L.S.; Shu, L.W.; Zhang, C.; Ouyang, Y.P. Geological Characteristics and Metallogenic Background of Zhuxi Tungsten (Copper) Polymetallic Deposit in the Eastern Part of the Yangtze River. *Chin. Sci. Geosci.* **2015**, *45*, 1799–1818, (In Chinese with English Abstract).
52. Li, Y.; Pan, X.F.; Zhao, M.; Cheng, G.H.; Zhang, T.F.; Liu, Q.; Zhang, C. Zircon U-Pb age and geochemical characteristics of granite porphyry in Zhuxi Tungsten (Copper) Deposit, Jingdezhen, and their relationship with mineralization. *Geol. Rev.* **2014**, *60*, 693–708, (In Chinese with English Abstract).
53. Li, C.H. Geochronology and Metallogenic Mechanism of Tungsten Deposits in the Northeastern Part of the Southeastern Margin of the Yangtze Plate. Ph.D. Dissertation, Nanjing University, Nanjing, China, 2016. (In Chinese with English Abstract).
54. Zhag, J.J.; Mei, Y.P.; Wang, D.H.; Li, H. Isotopic chronology of the Xianglushan scheelite deposit in northern Jiangxi and its geological significance. *J. Geol.* **2009**, *82*, 927–931, (In Chinese with English Abstract).
55. Yang, J.H.; Cheng, X.Y.; Wang, X.D. Geochronology of granites and geochemistry of ore-forming fluids in Dangping tungsten deposit, Jiangxi Province. *J. Miner.* **2009**, *29*, 339–340, (In Chinese with English Abstract).
56. Wu, F.Y.; Lin, J.Q.; Wilde, S.A.; Zhang, X.O.; Yang, J.H. Nature and significance of the Early Cretaceous giant igneous event in eastern China. *Earth Planet. Sci. Lett.* **2005**, *233*, 103–119. [[CrossRef](#)]
57. Ertel, W.; O'Neill, H.S.C.; Dingwell, D.B.; Spettel, B. Solubility of tungsten in a haplobasaltic melt as a function of temperature and oxygen fugacity. *Geochim. Cosmochim. Acta* **1996**, *60*, 1171–1180. [[CrossRef](#)]
58. He, M.; Zheng, H.; Clift, P.D. Zircon U-Pb geochronology and Hf isotope data from the Yangtze River sands: Implications for major magmatic events and crustal evolution in Central China. *Chem. Geol.* **2013**, *360–361*, 186–203. [[CrossRef](#)]
59. Sun, W.D.; Huang, R.F.; Li, H.; Hu, Y.B.; Zhang, C.C.; Sun, S.J.; Zhang, L.P.; Ding, X.; Li, C.Y.; Zartman, R.E. Porphyry deposits and oxidized magmas. *Ore Geol. Rev.* **2015**, *65*, 97–131. [[CrossRef](#)]
60. Jugo, P.; Candela, P.; Piccoli, P. Magmatic sulfides and Au: Cu ratios in porphyry deposits: An experimental study of copper and gold partitioning at 850 °C, 100 MPa in a haplogranitic melt–pyrrhotite–intermediate solid solution–gold metal assemblage, at gas saturation. *Lithos* **1999**, *46*, 573–589. [[CrossRef](#)]
61. Qiu, J.T.; Yu, X.Q.; Santosh, M.; Zhang, D.H.; Chen, S.Q.; Li, P.J. Geochronology and magmatic oxygen fugacity of the Tongcun molybdenum deposit, northwest Zhejiang, SE China. *Miner. Depos.* **2013**, *48*, 545–556. [[CrossRef](#)]
62. Vigneresse, J.L. The role of discontinuous magma inputs in felsic magma and ore generation. *Ore Geol. Rev.* **2007**, *30*, 181–216. [[CrossRef](#)]
63. Richards, J.P. The oxidation state, and sulfur and Cu contents of arc magmas: Implications for metallogeny. *Lithos* **2015**, *233*, 27–45. [[CrossRef](#)]
64. Wang, F.Y.; Ling, M.X.; Ding, X.; Hu, Y.H.; Zhou, J.B.; Yang, X.Y.; Liang, H.Y.; Fan, W.M.; Sun, W. Mesozoic large magmatic events and mineralization in SE China: Oblique subduction of the Pacific plate. *Int. Geol. Rev.* **2011**, *53*, 704–726. [[CrossRef](#)]



© 2020 by the authors. Licensee MDPI, Basel, Switzerland. This article is an open access article distributed under the terms and conditions of the Creative Commons Attribution (CC BY) license (<http://creativecommons.org/licenses/by/4.0/>).